



# Modelling disc-brake squeal in a multi-body-dynamics environment

## **Diplomarbeit**

zur Erlangung des akademischen Grades

Diplom-Ingenieur

an der Technischen Universität Wien,

Fakultät für Maschinenbau,

Institut für Mechanik und Mechatronik E325

Betreuer

Priv.-Doz. Dipl.-Ing. Dr.techn. Johannes Edelmann

Ao.Univ.Prof. Dipl.-Ing. Dr.techn. Manfred Plöchl

eingereicht von

**Ivo Sebastian Steinbrecher**

Matrikelnummer e0927253

Wien, am 16. Juni 2015

Ivo Sebastian Steinbrecher

*Für meinen Vater Günter Steinbrecher*

# Erklärung zur Verfassung dieser Arbeit (German)

Ivo Sebastian Steinbrecher  
Südtirolerplatz 2/26, 1040 Wien

Ich habe zur Kenntnis genommen, dass ich zur Drucklegung meiner Arbeit unter der Bezeichnung **Diplomarbeit** nur mit Bewilligung der Prüfungskommission berechtigt bin.

Ich erkläre weiter an Eides statt, dass ich meine Diplomarbeit nach den anerkannten Grundsätzen für wissenschaftliche Abhandlungen selbstständig ausgeführt habe, und alle verwendeten Hilfsmittel, insbesondere die zugrunde gelegte Literatur, genannt habe.

Des Weiteren erkläre ich, dass ich dieses Diplomarbeitsthema bisher, weder im In- noch Ausland (einer Beurteilerin/einen Beurteiler zur Begutachtung), noch in irgendeiner Form als Prüfungsarbeit vorgelegt habe, und dass diese Arbeit mit der vom Begutachter beurteilten Arbeit übereinstimmt.

Wien, 16. Juni 2015

Ivo Sebastian Steinbrecher

## Danksagung (German)

Mein Dank gilt hier allen voran meinen Betreuern Priv.-Doz. Dipl.-Ing. Dr.techn. Johannes EDELMANN und Ao.Univ.Prof. Dipl.-Ing. Dr.techn. Manfred PLÖCHL, die sich immer Zeit für mich genommen und mir in den gemeinsamen Gesprächen mit Rat und Tat zur Seite gestanden haben. Des Weiteren wäre ohne Univ.Prof. Dipl.-Ing. Dr.techn. Manfred KALTENBACHER und Univ.Ass. Dr.techn. Andreas HÜPPE die akustische Finite-Elemente Rechnung nicht zustande gekommen.

Ein großes Dankeschön gilt meiner gesamten erweiterten Familie, die mich im Laufe meines Lebens und Studiums immer unterstützt hat, vor allem meine Mutter Elke STEINBRECHER und meiner Freundin Theresa REIMOSER.

Ebenso kommt auch meinen Studienfreunden Christof BINDER, Benjamin HACKL, Bernhard HOPFNER, Andreas KALTENBRUNNER, Ferdinand PACHER und Stefan SCHODER Dank hinzu, da sie mir mit fachlichem Rat und Diskussionen zur Seite gestanden und meine Studentenzzeit um einiges bereichert haben.

Zuletzt möchte ich noch Robert BINDER und Martin HASLINGER danken, die mir geholfen haben bereits in jungen Jahren meine Begeisterung für den Maschinenbau zu entdecken, nicht zu vergessen, mein HTL-Professor Dipl.-Ing. Rudolf HAMETNER, der mir die Mechanik näher bringen konnte und meine Leidenschaft für diese Thematik geweckt hat.

# Abstract

Brake squeal is known to be an issue at disc brakes since their introduction, but a complete understanding of the problem is still missing. Experiments show that transversal vibrations of the brake disc are responsible for squeal. In literature, different sources of the instabilities that lead to squeal are discussed. In this thesis self-excited vibrations due to the follower-force characteristic of the friction forces are investigated.

Different analytical minimal models for disc-brake squeal are introduced, and two are discussed in detail. One model uses a rigid disc with friction contact, the second one uses a flexible disc with two eigenmodes of the disc. Current numerical simulations are based on full finite-element models of the brake system. This approach has the disadvantage of a high computational effort and only gives limited information about the squeal process itself. In this thesis a rigid- and a flexible-disc model are modelled and analysed in the multi-body-system program *SIMPACK*. The advantage of this approach is the computational efficiency and the chance to expand the model easily in order to represent more complex systems. Finally, the potential of the combination of multi-body-system dynamics and acoustic finite-element analysis is demonstrated.

In order to model the flexible disk in *SIMPACK*, a finite-element model of the has been pre-processed for the multi-body-system dynamics analysis. The needed mechanical mathematical foundations are explained.

# Zusammenfassung (German)

Das Bremsscheibenquietschen ist ein allseits bekanntes Phänomen, welches schon seit dem Beginn der Verwendung von Scheibenbremsen vor über 100 Jahren vorhanden ist. Dennoch gibt es noch kein geschlossenes Berechnungsmodell, um dieses Quietschen zu modellieren, vorherzusagen und ultimativ zu unterbinden. Experimente zeigen, dass transversale Schwingungen der Bremsscheibe für das Quietschen verantwortlich sind. In der Literatur gibt es unterschiedliche Ansichten, aufgrund welches Mechanismus die Instabilitäten auftreten, die zum Quietschen führen. In dieser Arbeit werden selbsterregte Schwingungen der Bremsscheibe untersucht, welche aufgrund der Folgelast-Eigenschaften der Reibungskräfte entstehen.

Es werden einige analytische Modelle vorgestellt; auf zwei davon wird im Detail eingegangen. Ein Modell verwendet eine starre Scheibe unter Reibkontakt und zeigt, dass auch bei dieser Instabilitäten auftreten können; das zweite Modell beschreibt die Bremsscheibe mit zwei Eigenmodes der Scheibe. Aktuelle numerische Ansätze bestehen meist aus komplexen Finite-Elemente-Analysen, welche sehr rechenaufwendig sind und nur bedingt Aufschlüsse über die Vorgänge beim Quietschen geben. In dieser Arbeit werden die analytischen Modelle mit dem Mehrkörpersystemdynamik-Programm *SIMPACK* modelliert und analysiert. Die Vorteile dieser Herangehensweise bestehen in der drastisch verkürzten Rechenzeit, sowie der leichten Adaptierbarkeit auf komplexere Systeme. Abschließend wird das Potential der Kombination von Mehrkörpersystemdynamik und akustischen Finite-Elemente-Analysen aufgezeigt.

Um die flexible Scheibe in *SIMPACK* modellieren zu können, muss diese aus einem Finite-Elemente-Modell für das Mehrkörpersystemdynamik-Programm vorbereitet werden. Die mechanisch-mathematischen Grundlagen dafür werden erläutert.

# Contents

<b>1. Introduction</b>	<b>1</b>
1.1. Structure of this thesis . . . . .	2
<b>2. Disc-brake squeal</b>	<b>3</b>
2.1. Mechanisms . . . . .	3
2.2. Minimal models . . . . .	3
2.3. Friction modelling . . . . .	6
2.4. Contact . . . . .	6
2.4.1. Contact modelling in the MBS environment . . . . .	6
<b>3. Rigid-disc model</b>	<b>8</b>
3.1. Analytical solution . . . . .	8
3.2. MBS simulation . . . . .	9
3.2.1. Modelling . . . . .	10
3.2.2. Eigenvalues . . . . .	11
<b>4. Flexible bodies in MBS</b>	<b>12</b>
4.1. FE preparation for flexible bodies . . . . .	15
4.1.1. Modelling . . . . .	15
4.1.2. Dynamic substructuring . . . . .	15
4.1.3. Output of the FE analysis . . . . .	17
4.2. MBS preprocessing of flexible bodies . . . . .	17
4.2.1. Orthogonalisation of the reduced system . . . . .	17
4.2.2. Mode shifting . . . . .	18
4.2.3. Constrained eigenmodes . . . . .	19
4.2.4. Interface modes . . . . .	20
4.2.5. Final equations of motion . . . . .	22
4.3. Preparing a FE beam for MBS simulation . . . . .	22
4.3.1. Example beams . . . . .	23
4.3.2. FE preparation . . . . .	23
4.3.3. Preprocessing for the MBS analysis . . . . .	26
<b>5. Flexible-disc model</b>	<b>36</b>
5.1. Analytical solution . . . . .	37
5.2. Natural frequencies of a transversely vibrating disc . . . . .	38
5.2.1. Effect of shear flexibility . . . . .	39

5.3.	MBS simulation . . . . .	40
5.3.1.	Modelling . . . . .	40
5.3.2.	FE mesh for the disc . . . . .	41
5.3.3.	Eigenvalues . . . . .	41
5.3.4.	Transient analysis . . . . .	43
5.4.	Acoustic simulation . . . . .	45
5.4.1.	FE model . . . . .	45
5.4.2.	Results . . . . .	47
<b>6.</b>	<b>Conclusion and outlook</b>	<b>50</b>
<b>A.</b>	<b><i>SIMPACK</i></b>	<b>52</b>
<b>B.</b>	<b>Transformation of coordinates</b>	<b>53</b>



# 1. Introduction

Brake squeal is known to be an issue at disc brakes since their introduction. Today this phenomenon is mainly a comfort problem and does not affect the functioning of the brakes themselves, but it is still an important issue for brake manufacturers and the automotive industry [1]. Lots of work has been published on this topic, but a complete understanding of the problem is still missing [2]. Since the development process of brake systems is an extensive and complex one, a reliable mathematical model of the squeal process is a valuable tool especially in the early development stages. In order to create such a model, the mathematical and mechanical understanding of the contact mechanism, the non-linear dynamics and the interactions of the brake system with the suspension system is essential [1, 2].

Disc-brake squeal is categorised as a high-frequency noise in the range of 1–16 kHz [3]. At lower frequencies other phenomena occur such as judder, groan moan, and howl, which are also sources of brake noise. Because of its high frequency, brake squeal is the most irritating of those noises and therefore the one on which most research work is concentrated [3]. Experiments show that transversal vibrations of the brake disc are responsible for squeal [1]. It is widely accepted that brake squeal occurs due to an instability caused by self-excited vibrations [4]. In literature, three basic sources of self-excited vibrations are discussed: stick-slip vibrations [5], negative gradient of the friction coefficient [6], and instability due to the follower-force characteristic of the friction forces. Chapter 2 gives a more detailed description of these different mechanisms. Reasons are given why the follower-force characteristic of the friction forces is assumed to be the governing mechanism behind brake squeal, opposed to stick-slip effects and a velocity-dependent friction coefficient.

Currently, there are two different ways of modelling brake squeal. One is to create a full finite-element (FE) model of the system with a large number of degrees of freedom (DOF) and to perform a complex eigenvalue analysis. The other method is to create minimal models with a considerably reduced amount of DOF which consist of mainly rigid bodies and in some cases include analytical formulations for the flexible deformations of the disc [1]. Both methods have their advantages and disadvantages. The FE models give results for complex loads and geometries of the brake system, but are computationally expensive. The simple models are useful to understand the general behaviour of the system, but lack the desired usability for commercial applications.

Both methods described above are well established and are currently used side by side, with the disadvantage that a direct relation between a complex FE model and a minimal model is missing. A promising approach is the combination of the two methods in one model. In order to do so, a proper framework is needed. Measurements show that brake-disc vibrations are the only important elastic vibrations for squeal; therefore, most other parts such as the brake pads or the sus-

pension may be modelled as rigid bodies. Considering those preconditions, multi-body systems (MBS) seem to be the logical choice. Before a full brake system can be analysed, it is important that the main mechanism behind disc-brake squeal is modelled and understood correctly. For reasons described in this thesis, the mechanism behind the rigid- and flexible-disc models from [1, 4] seems to be the most promising one. Therefore, the goal is to model the rigid- and flexible-disc models in a MBS environment, in this case the commercial software package *SIMPACK*, and to investigate the usability of this approach. If the fundamental mechanism can be modelled in MBS, the extension of the simple minimal models to more complex and realistic systems can be done with reasonable effort.

The simulation in MBS is a lot faster than a full FE analysis of a brake system, and transient solutions are easy to obtain as well. This allows for a subsequent acoustic FE simulation with the data generated from the MBS analysis. With the data generated from the acoustic solution, the sound emission of the brake system can be studied in detail.

## **1.1. Structure of this thesis**

The thesis is structured as follows: In Chapter 2 basic mechanisms of disc-brake squeal will be addressed. The model presented in [4] will be studied in detail, as well as modelled in MBS in Chapter 3. Chapter 4 will state the basic procedure to implement flexible bodies into MBS simulations, and give simple examples to illustrate the methods used. In Chapter 5 the model given in [1] will be studied in detail, as well as modelled in MBS. An acoustic FE simulation of the flexible disc will also be performed. A conclusion and outlook on this thesis will be given in Chapter 6.

## 2. Disc-brake squeal

### 2.1. Mechanisms

As stated in the introduction, different mechanisms for disc-brake squeal are discussed in literature:

**Stick-slip** When the relative velocity between two friction pairs becomes zero, the components stick to each other due to the coefficient of static friction  $\mu_s$  being higher than the coefficient of sliding friction  $\mu_k$ . The spectrum of those vibrations can include some frequencies noticeable by the human ear [5].

**Velocity dependent coefficient of friction** Experiments have shown that the coefficient of sliding friction  $\mu_k$  is a function of the relative velocity  $v_r$  between the contact points. A typical curve for  $\mu_k(v_r)$  as used in [6] is shown in Figure 2.1a. It can be observed that the curve has a negative gradient at low values of  $v_r$ . This can lead to a negative damping term in the linearised equations of motion and therefore to instability.

**Non-conservative friction forces** Normal forces act perpendicular to the contact surface and therefore have follower-force characteristics, as do the friction forces. Follower forces are known to be non-conservative and therefore do not have a potential. This leads to a non-symmetric stiffness matrix and for particular parameter constellations this can cause mode coupling instability or flutter [4].

### 2.2. Minimal models

Minimal models are of interest as they should be able to model the disc-brake phenomenon as simply as possible in order to study the governing physical mechanisms. A lot of models available in literature use one or more of the mechanisms described above. The model by SHIN *et al.* is given in [6] and shown in Figure 2.1b. This model uses a varying coefficient of friction shown in Figure 2.1a. POPP *et al.* [7] introduce a two DOF model shown in Figure 2.2. This model uses a constant coefficient of friction. The resulting stiffness matrix is non-symmetric and therefore instabilities can occur. In [8], BROMMUNDT introduces a three DOF model shown in Figure 2.3. This model uses a varying friction coefficient, but the curve is monotonically increasing. Again, instabilities occur because of the non-symmetric stiffness matrix.

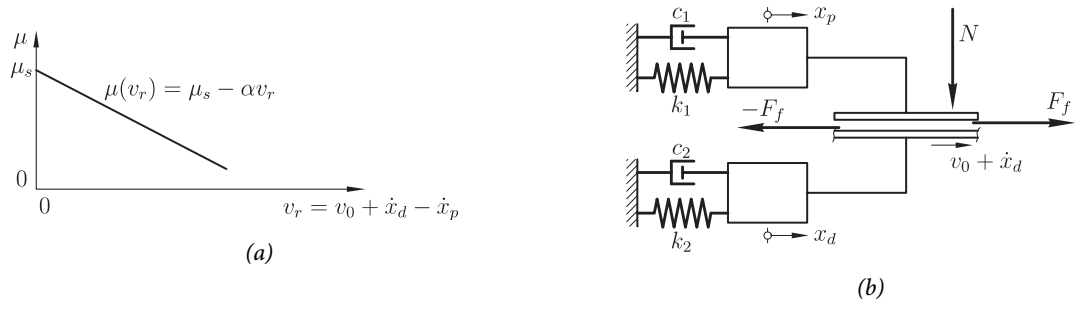


Figure 2.1.: (a) Friction characteristic used by the SHIN model [4]. (b) Model by SHIN *et al.* [4].

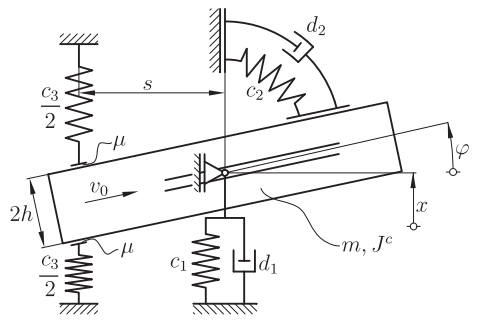


Figure 2.2.: Model by POPP *et al.* [4].

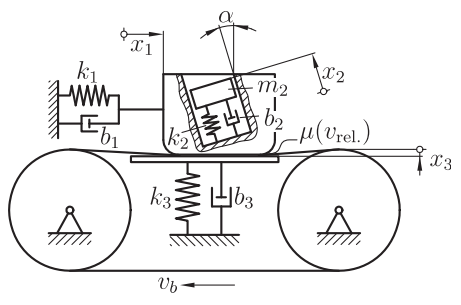


Figure 2.3.: Model by BROMMUNDT [4].

Those models have in common that they lack a connection to real brake systems and it can be difficult to interpret the parameters used in the models. Experiments show that transversal vibrations of the disc are the source of the squeal sound [9]. Therefore, models which are able to show those vibrations are of interest. In [4], VON WAGNER *et al.* introduce a minimal model for disk brake squeal using a rigid disk with two DOF, shown in Figure 2.4. The model uses a constant coefficient of friction and the instabilities occur because of the non-conservative friction forces that lead to a non-symmetric stiffness matrix. In [9], HOCHLENERT *et al.* give a similar model that uses a flexible disk with two modal DOF shown in Figure 2.5. The clear advantage of those two models is that they resemble a real disk brake system in a simple way. Those models are used to model disc-brake squeal in the MBS environment in this thesis.

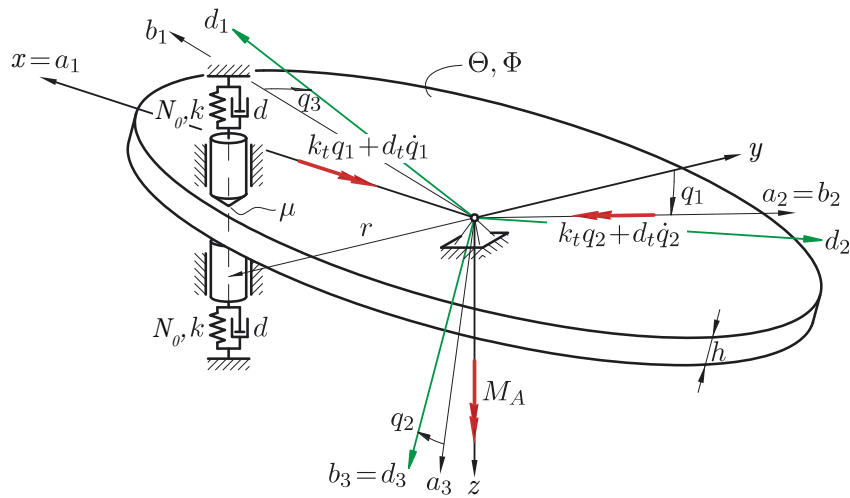


Figure 2.4.: Rigid-disc model by VONWAGNER *et al.* [4].

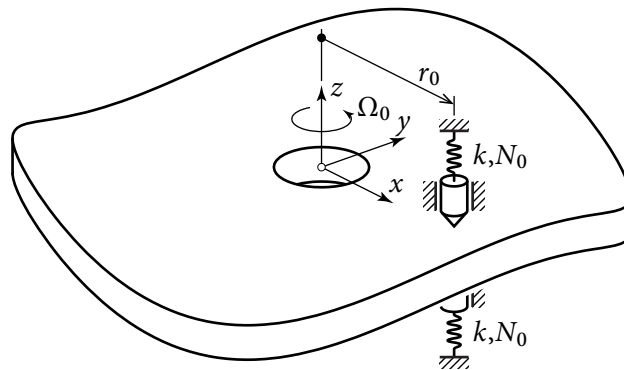


Figure 2.5.: Flexible-disc model by HOCHLENERT *et al.*.

## 2.3. Friction modelling

Both the rigid- and flexible-disc models use the COULOMB friction law

$$\vec{R} = -\mu \|\vec{N}\| \frac{\vec{v}_r}{\|\vec{v}_r\|}. \quad (2.1)$$

The direction of the friction force  $\vec{R}$  is in the opposite direction of the relative velocity  $v_r$  of the contact points and the magnitude is proportional to the normal force  $\vec{N}$ . Stick-slip effects are omitted as it is assumed that on a macroscopic scale the contact points never have zero relative velocity. This assumption is valid for the parameters used, in the models [1]. The velocity-dependent coefficient of friction is also not included in the models used as the change in relative velocity is so small that the corresponding change in the coefficient of friction would not have a noticeable effect on the results [1].

## 2.4. Contact

To simulate self-excited vibrations due to follower forces, the correct modelling of the forces is essential and in case of the brake disc it depends on the contact formulation between the disc and the brake pads. The analysed models in this thesis use point contacts between the upper and lower brake pad and the disc. This is of course an assumption and does not fully describe the surface-to-surface contact that occurs in reality, but for the purpose of the models the assumption is valid.

### 2.4.1. Contact modelling in the MBS environment

Only point contacts between pad and disc are assumed, which simplifies the contact modelling in MBS significantly compared to a surface-to-surface contact. Still, the way the contact is implemented is of high importance since system behaviour is highly dependent on the contact forces. Therefore, it is necessary to model the contact exactly as it is assumed in the analytical models given in [1, 4]. For example, an intuitive assumption could be that the friction force only acts in circumferential direction, which is easy to implement in MBS. The authors in [9] state that the small relative velocities between the contact point on the disc and pad in radial direction are important for the stability analysis and should not be neglected. Therefore the friction force has to be exactly opposed to the direction of the relative velocity, rather than only in circumferential direction. It is also assumed that no gap occurs between the contact pair, which is a valid assumption for a brake process [1].

The contact used can be reduced to the intersection of a plane and a line, with the contact planes being the upper and lower disc surfaces and the line being the axis of the brake pads. The contact geometry is shown in Figure 2.6. This illustration is valid for all contact planes that are not parallel to  $\vec{e}_z$ . In the MBS simulation a dummy body with neglectable mass properties and the local

coordinate system  $\vec{a}_{1-3}$  is added. The movement of the dummy is restricted to translations in  $z$  and rotations about  $\vec{e}_x$  and  $\vec{e}_y$  ( $\alpha$  and  $\beta$ ), therefore the  $\vec{a}_1$  vector always lies in the  $\vec{e}_x$ - $\vec{e}_z$  plane. The vectors  $\vec{b}_{1-3}$  represent a Cartesian coordinate system where  $\vec{b}_3$  is the normal vector of the contact plane. Finally, the vectors  $\vec{a}_1$  and  $\vec{a}_2$  are constrained with respect to  $\vec{b}_{1-3}$  in  $z$  direction as well as rotations in  $\alpha$  and  $\beta$ . Therefore, the constraint force of the  $z$ -constraint is also the normal force between the contact pair and can directly be used for the modelling of the friction force. The final position of the reference frame of the dummy body is in the contact point as well as parallel to the contact plane.

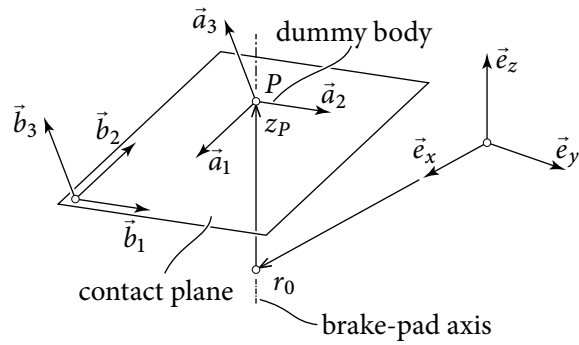


Figure 2.6.: Contact geometry used in the MBS model.

### 3. Rigid-disc model

The first model analysed is the rigid-disc model shown in Figure 2.4. It consists of a rigid disc with the mass moments of inertia  $\Theta$  w.r.t. to the local  $x$  and  $y$  axis and  $\Phi$  w.r.t. the local  $z$  axis. The disc is supported by a spherical joint in its centre. At a distance  $r_0$  in negative  $y$  direction there are two brake pads that are in point contact with the disc. COULOMB friction is assumed with the friction coefficient  $\mu$ . The brake pads are connected to the inertial system by a spring-damper system with the parameters  $k$  and  $d$  and are a preloaded by the force  $N_0$ . In the centre, the disc is coupled to the inertial system by two pairs of rotational spring-damper systems with the parameters  $k_t$  and  $d_t$ . Also on the centre of the disc there acts a moment  $M_A$  to ensure a constant angular velocity  $\Omega_0$  of the disc in  $z$  direction. The value of the moment is calculated by [4]

$$M_A = 2\mu r_0 N_0. \quad (3.1)$$

Therefore the model has two DOF,  $q_1$  and  $q_2$ .

#### 3.1. Analytical solution

The equations of motion for the linearised system are given in [4]

$$\begin{pmatrix} \Theta & 0 \\ 0 & \Theta \end{pmatrix} \begin{bmatrix} \ddot{q}_1 \\ \ddot{q}_2 \end{bmatrix} + \begin{pmatrix} \frac{1}{2}\mu N_0 \frac{h^2}{r_0 \Omega_0} + 2dr_0^2 & \Phi \Omega_0 \\ -\Phi \Omega_0 - \mu dhr_0 & d_t \end{pmatrix} \begin{bmatrix} \dot{q}_1 \\ \dot{q}_2 \end{bmatrix} + \begin{pmatrix} k_t + 2kr_0^2 + N_0h & \frac{1}{2}\mu N_0 \frac{h^2}{r} \\ -\mu(khr_0 + 2N_0r_0) & k_t + (1 + \mu^2)N_0h \end{pmatrix} \begin{bmatrix} q_1 \\ q_2 \end{bmatrix} = \mathbf{0}. \quad (3.2)$$

It can be observed that the damping matrix has terms depending on the angular velocity  $\Omega_0$ , and as stated before, the stiffness matrix is non-symmetric. With the *ansatz*

$$\mathbf{q}(t) = \hat{\mathbf{q}}e^{\lambda t} \quad (3.3)$$

the equations of motion (3.2) read

$$(\lambda^2 \mathbf{M} + \lambda \mathbf{C} + \mathbf{K}) \hat{\mathbf{q}} = \mathbf{0}. \quad (3.4)$$

This system represents a quadratic eigenvalue problem for the eigenvalue  $\lambda$  and the eigenvector  $\hat{\mathbf{q}}$ . If the eigenvalue  $\lambda$  has a positive real part, the trivial solution becomes unstable as the *ansatz* (3.3) increases exponentially. This is the stability criterion for the linearised system. In [4], parameters for the rigid-disc model are given, see Table 3.1. The spring stiffness is chosen, so that



the eigenfrequencies of the rigid disc are in the same range as the eigenfrequencies of a flexible disc with similar measurements. Figure 3.1 shows the eigenvalues with positive imaginary part for an angular frequency  $\Omega_0$  between  $\pi \text{ s}^{-1}$  and  $20\pi \text{ s}^{-1}$ . One eigenvalue crosses the imaginary axis and becomes positive at  $\Omega_0 = 10.4\pi \text{ s}^{-1}$ , which is the critical angular velocity.

Table 3.1.: Parameters used for the rigid-disc model [4].

Parameter	Physical meaning	Unit	Value
$k_t$	rotational spring stiffness	Nm	$1.88 \cdot 10^7$
$d_t$	rotational damper coefficient	Nms	0.1
$k$	spring stiffness	N/m	$6 \cdot 10^6$
$d$	damper coefficient	Ns/m	5
$N_0$	preload force	N	3000
$\mu$	coefficient of friction	1	0.6
$r_0$	radius for brake pad	m	0.13
$h$	height of the disc	m	0.02
$\Theta$	mass moment of inertia w.r.t. $x$ and $y$	$\text{kg/m}^2$	0.16
$\Phi$	mass moment of inertia w.r.t. $z$	$\text{kg/m}^2$	0.32

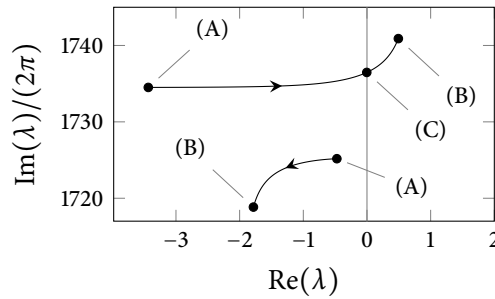


Figure 3.1.: Imaginary and real part of the eigenvalues for the linearised system of the rigid disc. The analytical solution is shown. The angular frequency  $\Omega_0$  varies from  $\pi \text{ s}^{-1}$  to  $20\pi \text{ s}^{-1}$ . Point (A) is calculated with  $\Omega_0 = \pi \text{ s}^{-1}$  and point (B) is calculated with  $\Omega_0 = 20\pi \text{ s}^{-1}$ . Point (C) is at  $\Omega_0 = 10.4\pi \text{ s}^{-1}$  and marks the point where the motion of the disc becomes unstable.

### 3.2. MBS simulation

*Note:* The terminology in this section refers to the MBS software package *SIMPACK*. For details see appendix A and [10].

### 3.2.1. Modelling

The disk is modelled as a rigid body and connected to the inertial system with a spherical joint. A force element is used to model the rotational springs between the inertial system and the disc. In *SIMPACK* the user is able to choose if the rotations are calculated linearised or non-linear with EULER angles. Both variants are used to calculate results. Another force element is used to apply the moment  $M_A$  that is required to keep a constant angular velocity  $\Omega_0$ . The contact is modelled as described in Section 2.4.1. The contact planes are fixed relatively to the disc and are parallel to the mid plane moved  $\pm h/2$  in local  $z$  direction. Force elements represent the spring-damper systems and the preload forces on the brake pads, as well as the friction forces acting on the brake pads and disc. The normal force for the friction force element is taken from the constraint connecting the dummy bodies to the contact plane. A marker on the disc is set congruent to the contact point but in the *SIMPACK* internal algorithms the relative velocity of this marker to the disc is set to zero, hence the marker represents a fixed point on the disc that is currently at the contact point. The relative velocity between this congruent marker and the contact point, is the friction velocity. It is used to calculate the direction of the friction force. It is important that the friction force is not only in circumferential direction as this leads to unusable results. For visualisation purposes, two bodies with neglectable mass properties are added to each dummy body, representing the brake pads. Figure 3.2 illustrates the MBS topology.

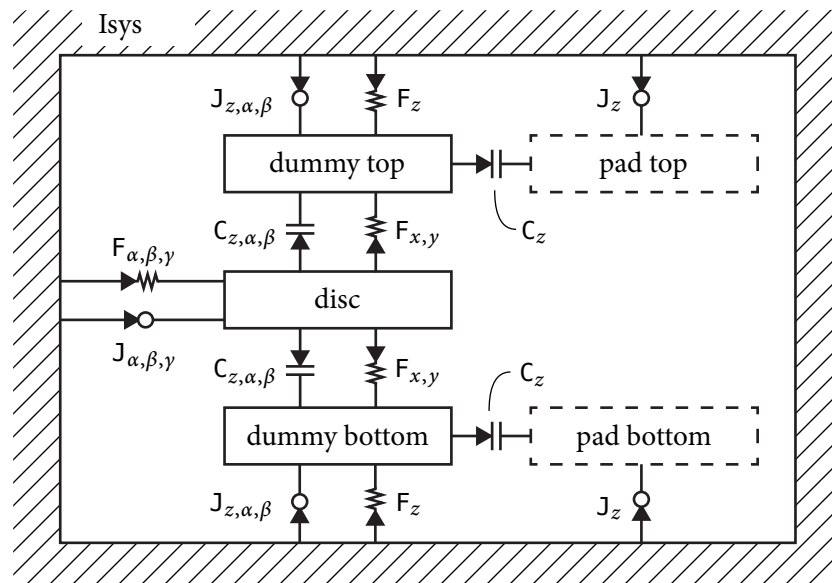


Figure 3.2.: Topology of the MBS rigid-disc model in *SIMPACK*.

### 3.2.2. Eigenvalues

To compare the analytical solution and the solution of the MBS model, the eigenvalues of the linearised system are analysed. Figure 3.3 shows the real and imaginary part of the analytical eigenvalues compared to the ones calculated in *SIMPACK*. The angular frequency  $\Omega_0$  is varied from  $\pi \text{ s}^{-1}$  to  $20\pi \text{ s}^{-1}$ . It can be seen that the results match very well. With linear angles the *SIMPACK* result is basically identical to the analytical solution. The result calculated with non-linear angles has minor discrepancies in the real part of the eigenvalues.

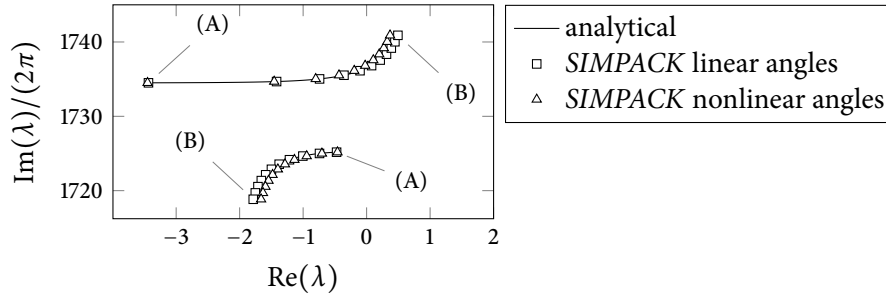


Figure 3.3.: Imaginary and real part of the eigenvalues for the linearised system of the rigid disc. The analytical as well as two different MBS results are shown. The angular frequency  $\Omega_0$  is varied from  $\pi \text{ s}^{-1}$  to  $20\pi \text{ s}^{-1}$ . Point (A) is calculated with  $\Omega_0 = \pi \text{ s}^{-1}$  and point (B) is calculated with  $\Omega_0 = 20\pi \text{ s}^{-1}$ .

## 4. Flexible bodies in MBS

If the dynamic response of the elastic deformations of a body have a relevant impact on the system, the assumption of applying only rigid bodies in MBS is not valid any more. In such a case the complete system can be modelled with FE using transient or harmonic analysis, giving the problem a high number of DOF. With this approach, little a priori knowledge about the form and type of the result is needed because the FE solution can project the solution to a large vector space that may give a good approximation of the exact solution. The obvious disadvantage of this method is the computational effort needed to get the solution. On the other hand the system can be modelled with MBS, by using additional DOF for the flexible parts. Each of those additional DOF scales a flexible displacement of the whole part; this displacement is called mode. This approach is based on the principle of modal superposition, which requires that the deformations of the structure can be described sufficiently with linear theory. In Figure 4.1, modal superposition is illustrated using the first two eigenmodes of a simple supported beam. In this case the beam has two generalised coordinates  $q_1$  and  $q_2$  corresponding to the first two eigenmodes  $\phi_1$  and  $\phi_2$ ; the final deformation of the beam is the superposition of those two modes scaled with the respective value of the DOF. The most intuitive set of usable modes are the eigenmodes of the body, but there are also other modes with certain advantages described in Section 4.2.4. The knowledge and experience of the user are essential for the selection of the additional DOF. This does not only refer to the number of modes selected but, more important, to which modes are selected. The goal is to use as few modes as necessary to keep the computational effort low but still represent the behaviour of the part in a sufficient way.

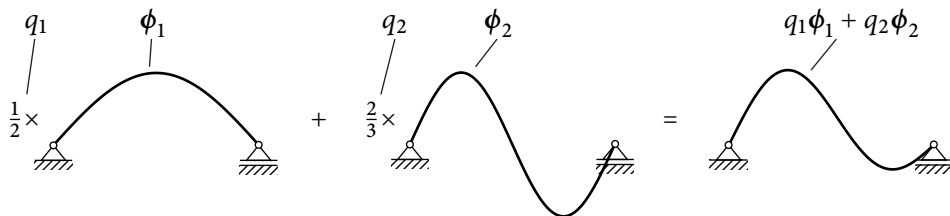


Figure 4.1.: Simple supported beam with superposition of two eigenmodes.

The elastic deformations are described with linear theory, but in the MBS simulation the flexible body can experience large non-linear displacements and rotations. To achieve this, the deformations of each body are described relative to a body reference frame, while this frame describes large displacements and rotations compared to other elements of the MBS analysis [11], see Figure 4.2. Each material point  $P$  on the undeformed body is described with a vector  $\vec{x}$  relative to the body reference frame. At time  $t$  the body is undeformed and the reference frame  $x_1, y_1$  is

described relative to the zero system  $x_0, y_0$  with the vector  $\vec{r}_{10}$  and rotation matrix  $\mathbf{R}$ . Therefore the absolute location of  $P$  is

$$\vec{r}_{P0} = \vec{r}_{10} + \mathbf{R}\vec{x}. \quad (4.1)$$

At time  $t_1$  the reference frame  $x'_1, y'_1$  is in a different position  $\vec{r}'_{1'0}$  and rotated with  $\mathbf{R}'$ . Now the body is deformed and/or moved relative to the body reference frame. Therefore the vector  $\mathbf{R}'\vec{x}$  does not point to the material point described by  $\vec{x}$ . The displacement of the point  $P'$  is  $\vec{u}(\vec{x}, t')$  relative to the reference frame. With this the position of  $P'$  is

$$\vec{r}_{P'0} = \vec{r}'_{1'0} + \mathbf{R}'\vec{x} + \mathbf{R}'\vec{u}(\vec{x}, t'). \quad (4.2)$$

This shows how large movement of a flexible body is described with only small deformations  $\vec{u}$ .

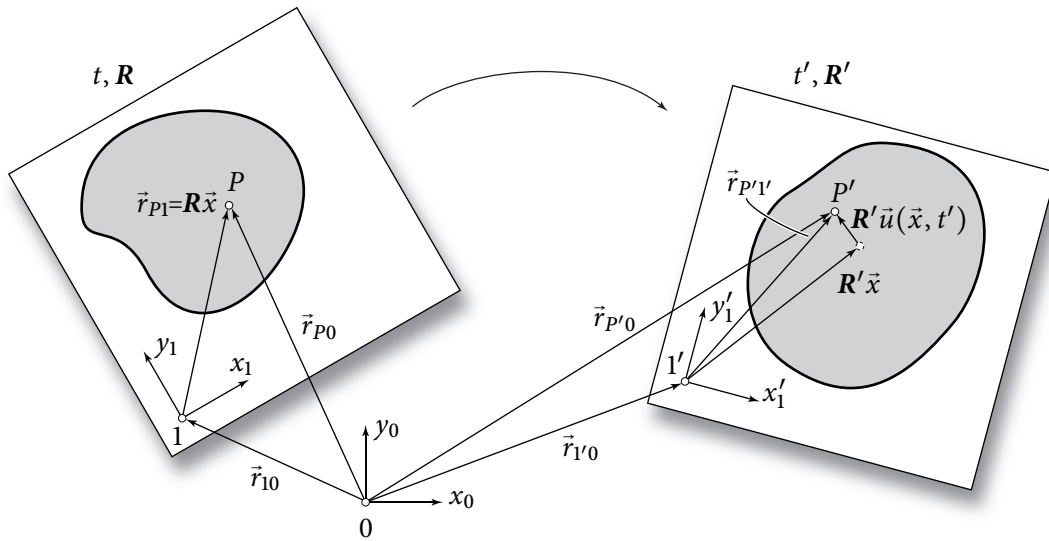


Figure 4.2.: Floating flexible body in two dimensions.

Besides implementation for simple beam elements, most commercial MBS software cannot pre-process complex flexible-body information for the MBS analysis. To get a reasonable accurate representation of the flexible body, FE software is used to create a reduced system that can be processed in MBS software. During this reduction process of a flexible body, the user is confronted with a lot of options and terminology that can exceed the average engineer's knowledge of FE and model reduction. User manuals of the software used are often short and inconclusive, but the quality of the result is highly dependent on the user making reasonable choices during the reduction process. To help for general understanding of this process, in the following, basic methods used for the reduction of a FE model and subsequent implementation into a MBS suitable formulation are described. It is not claimed that the described methods are the most efficient or most accurate ones, but rather an attempt to give the reader a basic knowledge of the reduction process itself. Figure 4.3 shows the workflow for implementing flexible bodies into MBS analysis using commercial software packages and the sections where detailed descriptions are given.

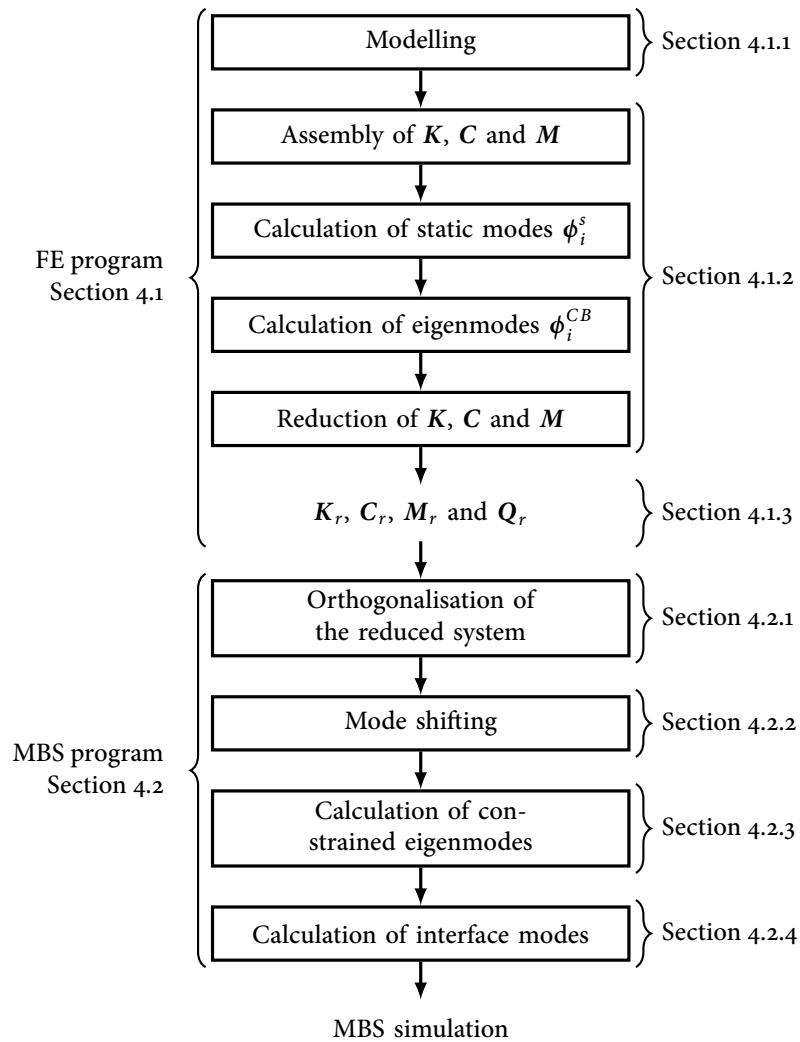


Figure 4.3.: Workflow for FE preparation of flexible bodies using the CRAIG-BAMPTON reduction method in the FE program and a MBS preprocessing similar to the one used in SIMPACK.

## 4.1. FE preparation for flexible bodies

### 4.1.1. Modelling

The modelling process is performed in a way that is similar to a linear FE analysis, that is choosing suitable element types and discretisations as well as defining possible material inhomogeneities and anisotropies. The main difference is the need for attachment points in the flexible body which can affect the setup of the mesh. In the final MBS model, loads and displacements can only be applied to specific nodes on the flexible body, so-called attachment points. This requires knowledge of those points at the time of the FE modelling, making contact problems a difficult task. Those problems can still be modelled by distributing the contact forces onto various attachment points. Since the number of attachment points influences the reduced system size for the flexible body, nodes on boundary or loading areas are often coupled to one attachment point. By doing this, the area only accounts for one attachment point, and forces in the MBS analysis can be distributed within this area. Depending on the substructuring method, the results can be improved by defining the boundaries acting on the MBS body in the FE model. The CRAIG–BAMPTON method [12], for example, cannot be improved by defining the correct boundary conditions in the model, since the eigenmodes are calculated for the substructure only. Also, it can be difficult to know the exact boundary conditions acting on the MBS model. In general, boundary conditions in the FE model should be applied according to the methods used and user experience.

### 4.1.2. Dynamic substructuring

FE software is better equipped to handle large matrices than MBS software. Since the number of DOF for a model can be in the range of  $10^6$ , it is necessary to reduce the amount of data given to the MBS preprocessor. This is done using dynamic substructuring for the FE model. The main idea is to divide the  $n$  nodes of a structure into  $n_m$  master and  $n_s$  slave nodes, then make the slave DOF dependent on the master DOF and reduce the assembled system matrices  $\mathbf{K}$ ,  $\mathbf{C}$  and  $\mathbf{M}$  to describe the equations of motion only for the masters, leading to a system with  $n_m$  DOF. Those master nodes are the attachment nodes used in the modelling. In the following sections two methods are described, the GUYAN reduction and the CRAIG–BAMPTON method. Both are so called displacement coupling methods as they couple the displacement of the interface nodes between the retained structure and substructure. Other methods might couple the forces and/or displacements at the interface.

#### Guyan reduction

In [13], it is proposed to first perform a static reduction and then reduce the mass and damping matrices with the same transformation. The vector of global generalised coordinates  $\mathbf{u}$  is given by

$$\mathbf{u} = \begin{bmatrix} \mathbf{u}_m \\ \mathbf{u}_s \end{bmatrix}, \quad (4.3)$$

where  $\mathbf{u}_m$  and  $\mathbf{u}_s$  are vectors containing the master and slave DOF, respectively. Now the static FE equation  $\mathbf{K}\mathbf{u} = \mathbf{f}$  can be written as

$$\begin{pmatrix} \mathbf{K}_{mm} & \mathbf{K}_{ms} \\ \mathbf{K}_{sm} & \mathbf{K}_{ss} \end{pmatrix} \begin{bmatrix} \mathbf{u}_m \\ \mathbf{u}_s \end{bmatrix} = \begin{bmatrix} \mathbf{f}_m \\ \mathbf{f}_s \end{bmatrix} \quad (4.4)$$

where  $\mathbf{K}_{ms} = \mathbf{K}_{sm}^T$ . Assuming that all external loads are applied on the masters,  $\mathbf{f}_s$  is equal to zero. Then, the lower set of equations in (4.4) can be solved for  $\mathbf{u}_s$ ,

$$\mathbf{u}_s = -\mathbf{K}_{ss}^{-1}\mathbf{K}_{sm}\mathbf{u}_m. \quad (4.5)$$

With this relation between the master and slave nodes, the slave nodes can be eliminated from Equation (4.4). This is done with the coordinate transformation

$$\mathbf{u} = \mathbf{Q}_G\mathbf{u}_m \quad \text{with} \quad \mathbf{Q}_G = \begin{pmatrix} \mathbf{I} \\ -\mathbf{K}_{ss}^{-1}\mathbf{K}_{sm} \end{pmatrix} \quad (4.6)$$

and the reduced system matrices are (see appendix B)

$$\mathbf{K}_r = \mathbf{Q}_G^T\mathbf{K}\mathbf{Q}_G \quad (4.7)$$

$$\mathbf{C}_r = \mathbf{Q}_G^T\mathbf{C}\mathbf{Q}_G \quad (4.8)$$

$$\mathbf{M}_r = \mathbf{Q}_G^T\mathbf{M}\mathbf{Q}_G. \quad (4.9)$$

Here the new coordinate vector is

$$\mathbf{q} = \mathbf{u}_m. \quad (4.10)$$

The reduced size of the system matrices is  $n_m \times n_m$ . A closer look at the matrix  $\mathbf{Q}_G$  reveals that the  $i$ th column of  $\mathbf{Q}_G$  represents a static mode  $\phi_i^s$  of the structure with a unit displacement at the  $i$ th master DOF and all other master nodes constrained.

### Craig–Bampton method

In the GUYAN reduction, only the static relation between  $\mathbf{u}_m$  and  $\mathbf{u}_s$  is taken into account, which can lead to poor accuracy for dynamic results. This can be improved by adding  $n_{CB}$  eigenvectors with the generalised coordinates  $\mathbf{q}^{CB}$  to the movement of the substructure [12], giving the CRAIG–BAMPTON method. It is not required that the  $n_{CB}$  eigenvectors are corresponding to the first  $n_{CB}$  eigenvalues. A term which represents the dynamic eigenvalues of the substructure is added to the approximation of the slave displacements in Equation (4.5)

$$\mathbf{u}_s = -\mathbf{K}_{ss}^{-1}\mathbf{K}_{sm}\mathbf{u}_m + \sum_i^{n_{CB}} q_i^{CB} \phi_i^{CB}. \quad (4.11)$$

$\phi_i^{CB}$  is the  $i$ th eigenvector for the undamped substructure, calculated with all master DOF constrained. This leads to a new coordinate transformation

$$\mathbf{u} = \mathbf{Q}_{CB} \begin{bmatrix} \mathbf{u}_m \\ \mathbf{q}^{CB} \end{bmatrix} \quad \text{with} \quad \mathbf{Q}_{CB} = \begin{pmatrix} \mathbf{I} & \mathbf{0} \\ -\mathbf{K}_{ss}^{-1}\mathbf{K}_{sm} & \mathbf{\Phi}_{CB} \end{pmatrix}. \quad (4.12)$$



Here  $\Phi_{CB}$  is a matrix where the  $i$ th column is the eigenvector corresponding to the generalised coordinates  $q_i$

$$\Phi_{CB} = (\phi_1^{CB}, \dots, \phi_{n_{CB}}^{CB}). \quad (4.13)$$

Finally the reduced system matrices including generalised coordinates are

$$\mathbf{K}_r = \mathbf{Q}_{CB}^T \mathbf{K} \mathbf{Q}_{CB} \quad (4.14)$$

$$\mathbf{C}_r = \mathbf{Q}_{CB}^T \mathbf{C} \mathbf{Q}_{CB} \quad (4.15)$$

$$\mathbf{M}_r = \mathbf{Q}_{CB}^T \mathbf{M} \mathbf{Q}_{CB}, \quad (4.16)$$

with the generalised coordinates

$$\mathbf{q} = \begin{bmatrix} \mathbf{u}_m \\ \mathbf{q}_{CB} \end{bmatrix}. \quad (4.17)$$

The reduced size of the system matrices is  $(n_m + n_{CB}) \times (n_m + n_{CB})$ .

### 4.1.3. Output of the FE analysis

The FE analysis output contains the reduced system matrices  $\mathbf{K}_r$ ,  $\mathbf{C}_r$  and  $\mathbf{M}_r$  and the transformation matrix  $\mathbf{Q}_{CB}$ . The reduced system matrices are of size  $n_{FE} \times n_{FE}$ , while the transformation matrix has size  $n \times n_{FE}$ , whereat  $n_{FE} = n_m + n_{CB}$  (in case of the CRAIG–BAMPTON method). Usually it can be said that  $n_{FE} \ll n$ , which means that the majority of data output contains entries for  $\mathbf{Q}_{CB}$ . Only the part of  $\mathbf{Q}_{CB}$  where the attachment points are described, is used in the MBS analysis. Other entries are for visualisation purposes only. To reduce the amount of output data, the transformation matrix could, for example, only describe the attachment points and the nodes on the outer surface of the body.

## 4.2. MBS preprocessing of flexible bodies

*Note:* From now on it is assumed that the CRAIG–BAMPTON method is used for the FE reduction.

In the previous section, the reduction of a FE model for a MBS analysis was described. It is common practice in MBS software to take the reduced system and calculate a new set of modes to be used in the analysis. In this chapter, a procedure similar to the one used in *SIMPACK* [10, 11] is described.

### 4.2.1. Orthogonalisation of the reduced system

Depending on the reduction method used, there can be the need for orthogonalisation of the reduced system. In case of the original CRAIG–BAMPTON method described in Section 4.1.2, there

are several disadvantages. That includes the superposition of rigid body modes in the CRAIG–BAMPTON modes and the dependency of the master node displacement on only one static mode. To avoid those problems, it is common to orthogonalise the reduced system. The eigenvalue problem of the undamped system

$$(-\omega_i^{e2} \mathbf{M}_r + \mathbf{K}_r) \boldsymbol{\phi}_i^e = \mathbf{0} \quad (4.18)$$

describes a free floating structure that can move and deform according to the modes used in the reduction process. The first  $n_r$  eigenvalues are zero with the corresponding eigenvectors representing the rigid body modes  $\boldsymbol{\phi}^r$ . Depending on the problem being planar or spatial,  $n_r$  can be either three or six. Those modes are calculated with

$$\mathbf{K}_r \boldsymbol{\phi}_i^r = \mathbf{0}. \quad (4.19)$$

The  $n_e$  non-zero eigenvalues of Equation (4.18) give the flexible eigenmodes  $\boldsymbol{\phi}^e$  of the free floating structure, since all eigenvalues are calculated  $n_e$  equals  $n_{FE} - n_r$ . This leads to a new vector of generalised coordinates

$$\mathbf{q}^e = [q_1^r, \dots, q_{n_r}^r, q_1^e, \dots, q_{n_e}^e]^T, \quad (4.20)$$

with the transformation matrix

$$\mathbf{Q}_e = \boldsymbol{\Phi}_e = (\boldsymbol{\phi}_1^r, \dots, \boldsymbol{\phi}_{n_r}^r, \boldsymbol{\phi}_1^e, \dots, \boldsymbol{\phi}_{n_e}^e). \quad (4.21)$$

The matrix  $\boldsymbol{\Phi}_e$  contains the eigenvectors of the rigid body modes and flexible eigenmodes. Therefore, the system matrices become

$$\mathbf{K}_e = \mathbf{Q}_e^T \mathbf{K}_r \mathbf{Q}_e \quad (4.22)$$

$$\mathbf{C}_e = \mathbf{Q}_e^T \mathbf{C}_r \mathbf{Q}_e \quad (4.23)$$

$$\mathbf{M}_e = \mathbf{Q}_e^T \mathbf{M}_r \mathbf{Q}_e, \quad (4.24)$$

with the coordinate transformation

$$\mathbf{u} = \mathbf{Q}_r \mathbf{Q}_e \mathbf{q}^e. \quad (4.25)$$

#### 4.2.2. Mode shifting

The system matrices in equations (4.22–4.24) describe a free floating beam that can move and deform with the independent modes in  $\boldsymbol{\Phi}_e$ . Depending on the structure of the model, it may be required to constrain the flexible body with respect to the body reference frame by locking  $n_c$  displacements or rotations. To fulfil the constraints,  $n_c$  modes of  $\boldsymbol{\Phi}_e$  are made dependent on the other modes. This is done by *mode shifting* [11]. In theory any modes can be chosen, but there are combinations of modes where the resulting system becomes ill-conditioned. A very suitable choice are the rigid body modes  $\boldsymbol{\phi}_i^r$  as they describe distortion-free movement of the flexible body. This is also a main reason for the orthogonalisation of the system in Section 4.2.1. The vector of generalised coordinates and the displacement vector are reordered so that the dependent coordinates and the constrained displacements are at the beginning. Reordering the Equation

(4.25) and assuming that all constrained displacements w.r.t. the reference frame are zero, leads to

$$\begin{bmatrix} \mathbf{0} \\ \mathbf{u}_u \end{bmatrix} = \begin{pmatrix} \mathbf{Q}_{dd} & \mathbf{Q}_{di} \\ \mathbf{Q}_{id} & \mathbf{Q}_{ii} \end{pmatrix} \begin{bmatrix} \mathbf{q}^d \\ \mathbf{q}^i \end{bmatrix}, \quad (4.26)$$

where  $\mathbf{Q}_{id} = \mathbf{Q}_{di}^T$ ,  $\mathbf{u}_u$  are the unconstrained displacements,  $\mathbf{q}^d$  are the dependent and  $\mathbf{q}^i$  the independent DOF. The first set of equations in Equation (4.26) solved for  $\mathbf{q}^d$  is

$$\mathbf{q}^d = -\mathbf{Q}_{dd}^{-1} \mathbf{Q}_{di} \mathbf{q}^i. \quad (4.27)$$

Now a coordinate transformation is introduced

$$\begin{bmatrix} \mathbf{q}^d \\ \mathbf{q}^i \end{bmatrix} = \mathbf{Q}_c \mathbf{q}^i \quad \text{with} \quad \mathbf{Q}_c = \begin{pmatrix} -\mathbf{Q}_{dd}^{-1} \mathbf{Q}_{di} \\ \mathbf{I} \end{pmatrix}. \quad (4.28)$$

This gives the transformed system matrices with the dimension  $(n_r - n_c) \times (n_r - n_c)$

$$\mathbf{K}_c = \mathbf{Q}_c^T \mathbf{K}_e \mathbf{Q}_c \quad (4.29)$$

$$\mathbf{C}_c = \mathbf{Q}_c^T \mathbf{C}_e \mathbf{Q}_c \quad (4.30)$$

$$\mathbf{M}_c = \mathbf{Q}_c^T \mathbf{M}_e \mathbf{Q}_c. \quad (4.31)$$

The final vector of generalised coordinates is  $\mathbf{q}^i$ , which can be transformed to the original displacements.  $\mathbf{u}$  reads

$$\mathbf{u} = \mathbf{Q}_r \mathbf{Q}_e \mathbf{Q}_c \mathbf{q}^i. \quad (4.32)$$

One might notice the similarity between the mode shifting and the GUYAN reduction. Basically, it is the same procedure: in the GUYAN reduction slave DOF are made dependent on master DOF, and in the mode shifting the same is done with dependent and independent modes.

### 4.2.3. Constrained eigenmodes

The current matrices  $\mathbf{K}_c$ ,  $\mathbf{C}_c$  and  $\mathbf{M}_c$  represent the full CRAIG–BAMPTON system, adjusted to the boundary conditions in the body reference frame. During the MBS preprocessing, it is common for the user to decide which modes to use in the final analysis. It is possible to choose a reduced set of modes in the orthogonalisation described in Section 4.2.1, but the free floating modes do not directly correspond to a constrained mode and it might be difficult to decide if the mode is relevant in the final analysis. Therefore, the eigenmodes to the constrained set equations are calculated. This is done with the eigenvalue problem of the undamped system,

$$(-\omega_i^c{}^2 \mathbf{M}_c + \mathbf{K}_c) \phi_i^c = \mathbf{0}. \quad (4.33)$$

Here  $\phi_i^c$  are the eigenmodes of the undamped system and  $\omega_i^c$  is the corresponding eigen angular frequency. The user can decide which modes are relevant for the final analysis and only use those. The  $n_h$  relevant modes build a transformation matrix  $\mathbf{Q}_h$

$$\mathbf{Q}_h = (\phi_1^h, \dots, \phi_{n_h}^h), \quad (4.34)$$

while the  $n_n$  neglected modes form  $\mathbf{Q}_n$

$$\mathbf{Q}_n = (\phi_1^n, \dots, \phi_{n_n}^n). \quad (4.35)$$

Here, the number of relevant and neglected modes is equal to the size of the system  $n_h + n_n = n_r - n_c$ . The transformation gives the system matrices only considering the relevant modes

$$\mathbf{K}_h = \mathbf{Q}_h^T \mathbf{K}_c \mathbf{Q}_h \quad (4.36)$$

$$\mathbf{C}_h = \mathbf{Q}_h^T \mathbf{C}_c \mathbf{Q}_h \quad (4.37)$$

$$\mathbf{M}_h = \mathbf{Q}_h^T \mathbf{M}_c \mathbf{Q}_h, \quad (4.38)$$

with the dimension  $n_h \times n_h$ . The vector of generalised coordinates is

$$\mathbf{q}^h = [q_1^h, \dots, q_{n_h}^h]^T \quad (4.39)$$

and can be transformed into the original displacements by

$$\mathbf{u} = \mathbf{Q}_r \mathbf{Q}_e \mathbf{Q}_c \mathbf{Q}_h \mathbf{q}^h. \quad (4.40)$$

#### 4.2.4. Interface modes

The accuracy of the solution depends on the number of used modes  $n_h$ . To improve the solution, more eigenmodes can be used for the simulation to extend the solution space, but this comes with the disadvantage of a higher computational effort. Instead of adding more eigenmodes to the simulation one can add *interface modes*. Interface modes are a superposition of the neglected modes and are calculated with the goal of retaining as much information from the neglected modes with as few interface modes as possible. Therefore, by using a few proper interface modes, the solution can be very similar to a solution using a lot of eigenmodes, but with applying fewer DOF.

To calculate the interface modes, the system is reduced with a coordinate transformation containing the neglected modes

$$\mathbf{Q}_n = (\phi_1^n, \dots, \phi_{n_n}^n). \quad (4.41)$$

Here the vector of generalised coordinates is

$$\mathbf{q}^n = [q_1^n, \dots, q_{n_n}^n]^T, \quad (4.42)$$

with the relation to the original displacements

$$\mathbf{u} = \mathbf{Q}_r \mathbf{Q}_e \mathbf{Q}_c \mathbf{Q}_n \mathbf{q}^n. \quad (4.43)$$

Therefore, the system matrices of the undamped system based on the neglected modes are

$$\mathbf{K}_n = \mathbf{Q}_n^T \mathbf{K}_c \mathbf{Q}_n \quad (4.44)$$

$$\mathbf{M}_n = \mathbf{Q}_n^T \mathbf{M}_c \mathbf{Q}_n, \quad (4.45)$$

with dimension  $n_n \times n_n$ . The interface modes in *SIMPACK* are calculated based on dynamic unit loads acting on the structure [11, 10].  $\mathbf{p}_k^r(t)$  is a load vector on the CRAIG–BAMPTON structure with a harmonic unit load in the  $k$  th row and can be written as

$$\mathbf{p}_k^r(t) = \mathbf{p}_k^r e^{i\Omega_0 t}, \quad (4.46)$$

where  $\Omega_0$  is the harmonic frequency of the unit load. Due to the construction of the CRAIG–BAMPTON method the  $k$  th row of  $\mathbf{p}_k$  corresponds to the  $k$  th master DOF, as long as  $k \leq n_m$ . With the previously used coordinate transformations, the load acting on the system based on the neglected modes is

$$\mathbf{p}_k^n = \mathbf{Q}_n^T \mathbf{Q}_c^T \mathbf{Q}_e^T \mathbf{p}_k^r. \quad (4.47)$$

This force applied to the undamped structure based on the neglected modes yields

$$\mathbf{M}_n \ddot{\boldsymbol{\phi}}_k^p(t) + \mathbf{K}_n \boldsymbol{\phi}_k^p(t) = \mathbf{p}_k^n e^{i\Omega_0 t}. \quad (4.48)$$

Here  $\boldsymbol{\phi}_k^p(t)$  is the interface mode for the  $k$  th master DOF. Since there is a harmonic excitation without damping, the interface mode can be written as  $\boldsymbol{\phi}_k^p(t) = \boldsymbol{\phi}_k^p e^{i\Omega_0 t}$ . This yields

$$(-\Omega_0^2 \mathbf{M}_n + \mathbf{K}_n) \boldsymbol{\phi}_k^p = \mathbf{p}_k^n. \quad (4.49)$$

The harmonic frequency  $\Omega_0$  can be chosen by the user. In [10] it is recommended to use half of the first non-zero eigenfrequency of the free floating structure. The frequency  $\Omega_0$  can also be zero. If that is the case, the interface modes are called *interface response modes (IRM)* and in the non-zero case *frequency response modes (FRM)*, see [10, 11]. In the following, only FRM are considered. The interface modes in Equation (4.49) can be considered as the response of the neglected modes to a unit load applied at one of the attachment points. Therefore, the interface modes have discontinuities in the section forces at the attachment points, which makes them more suitable than eigenmodes to represent dynamic loads on the structure. In *SIMPACK*, FRM modes can only be calculated for constrained<sup>1</sup> or loaded attachment points, which seems useful since those are the points at which external forces act on the structure. The calculated modes are assembled in the matrix

$$\mathbf{Q}_p = (\boldsymbol{\phi}_1^p, \dots, \boldsymbol{\phi}_{n_p}^p). \quad (4.50)$$

Here  $n_p$  is the number of calculated interface modes and the index  $i$  in  $\boldsymbol{\phi}_i^p$  refers to the  $i$  th calculated mode and not the one corresponding to a unit load at master node  $i$ . In order to add the interface modes to the coordinate transformation based on the eigenmodes of the constrained structure, the matrix  $\mathbf{Q}_p$  must be transformed for the generalised coordinates  $\mathbf{q}_c$ . Then this matrix and the transformation matrix with the relevant modes are added together, giving the final transformation matrix

$$\mathbf{Q}_m = (\mathbf{Q}_h, \mathbf{Q}_n \mathbf{Q}_p). \quad (4.51)$$

---

<sup>1</sup>In this case “constrained” refers to constraint elements used in *SIMPACK*. The boundaries imposed by mode shifting are given by the joint of the body and do not require FRM.

The corresponding system matrices are

$$\mathbf{K}_m = \mathbf{Q}_m^T \mathbf{K}_c \mathbf{Q}_m \quad (4.52)$$

$$\mathbf{C}_m = \mathbf{Q}_m^T \mathbf{C}_c \mathbf{Q}_m \quad (4.53)$$

$$\mathbf{M}_m = \mathbf{Q}_m^T \mathbf{M}_c \mathbf{Q}_m, \quad (4.54)$$

with the dimension  $(n_h + n_p) \times (n_h + n_p)$  and the generalised coordinate vector

$$\mathbf{q}^m = [q_1^h, \dots, q_{n_h}^h, q_1^p, \dots, q_{n_p}^p]^T. \quad (4.55)$$

This vector can be transformed into the original displacements with

$$\mathbf{u} = \mathbf{Q}_r \mathbf{Q}_e \mathbf{Q}_c \mathbf{Q}_m \mathbf{q}^m. \quad (4.56)$$

#### 4.2.5. Final equations of motion

The final equations of motion are

$$\mathbf{M}_m \ddot{\mathbf{q}}^m + \mathbf{C}_m \dot{\mathbf{q}}^m + \mathbf{K}_m \mathbf{q}^m = \mathbf{p}^m. \quad (4.57)$$

The load vector  $\mathbf{p}^m$  consists of transformed external loads as well as inertia forces resulting from the movement of the body reference frame [11]. Usually the damping term  $\mathbf{C}_m \dot{\mathbf{q}}^m$  in Equation (4.57) is replaced with modal damping [10]. The final matrices can vary depending on the amount of modes used and if the body is constrained, but in general, the procedure described in the previous sections is performed to get the final reduced matrices for the MBS analysis.

### 4.3. Preparing a FE beam for MBS simulation

In the previous two sections 4.1 and 4.2, basic methods for the reduction process of a flexible body into MBS are described. In this section, those methods are applied on two simple beams, in order to give the reader a demonstrative understanding of the methods in addition to the equations stated earlier. The *MATLAB* tool *MaxiFrame* developed at the *Section of Solid Mechanics* in the *Department of Mechanical Engineering* at the *Technical University of Denmark* is a linear static FE code for beam elements. This tool was used as a framework to implement the FE and MBS preprocessing of flexible bodies into *MATLAB*. Therefore, it is possible to show the steps from the FE model to the final MBS model in detail, which can hardly be done using commercial software due to the black-box character of such programs.

### 4.3.1. Example beams

Figure 4.4 shows the two example beams considered in this section. The first beam (a) is a cantilever beam with a harmonic moment acting at  $L/3$ , while the second one (b) is a simple supported beam with a harmonic force acting also at  $L/3$ . For both beams gravity is neglected and it is assumed that the beams only experience bending vibrations. The harmonic loads have the frequency  $\Omega$ .



(a) Cantilever beam with harmonic moment. (b) Simple supported beam with harmonic force.

Figure 4.4.: The two example problems.

### 4.3.2. FE preparation

The beams are modelled with 300 two-dimensional BERNOULLI–EULER beam elements. Since the longitudinal vibrations are not accounted for the FE code, the code is modified so that the beam elements have 2 DOF per node. This leaves the final FE model with 301 nodes and 602 DOF. Since all relevant points on the two beams are on the same position, the same FE model can be used for both examples. Dynamic substructuring is performed with the CRAIG–BAMPTON method, using three attachment points A, B and C, as they are the loading and boundary points. Figure 4.5 shows the numbering of the master DOF. Static modes  $\phi_i^s$  corresponding to those DOF are shown in Figure 4.6. Each mode  $\phi_i^s$  represents the static deformation for a unit displacement at master node  $i$  with all other master nodes constrained. Also used for substructuring are the first 100 eigenmodes, calculated with all master DOF constrained. The first 8 eigenmodes are shown in Figure 4.7. With the transformations described in Section 4.1.2, this gives the reduced system matrices the dimension  $106 \times 106$ . The global system matrices can now be preprocessed for the MBS simulation.

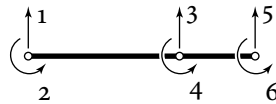


Figure 4.5.: Numbering of the master DOF for the reduced model.

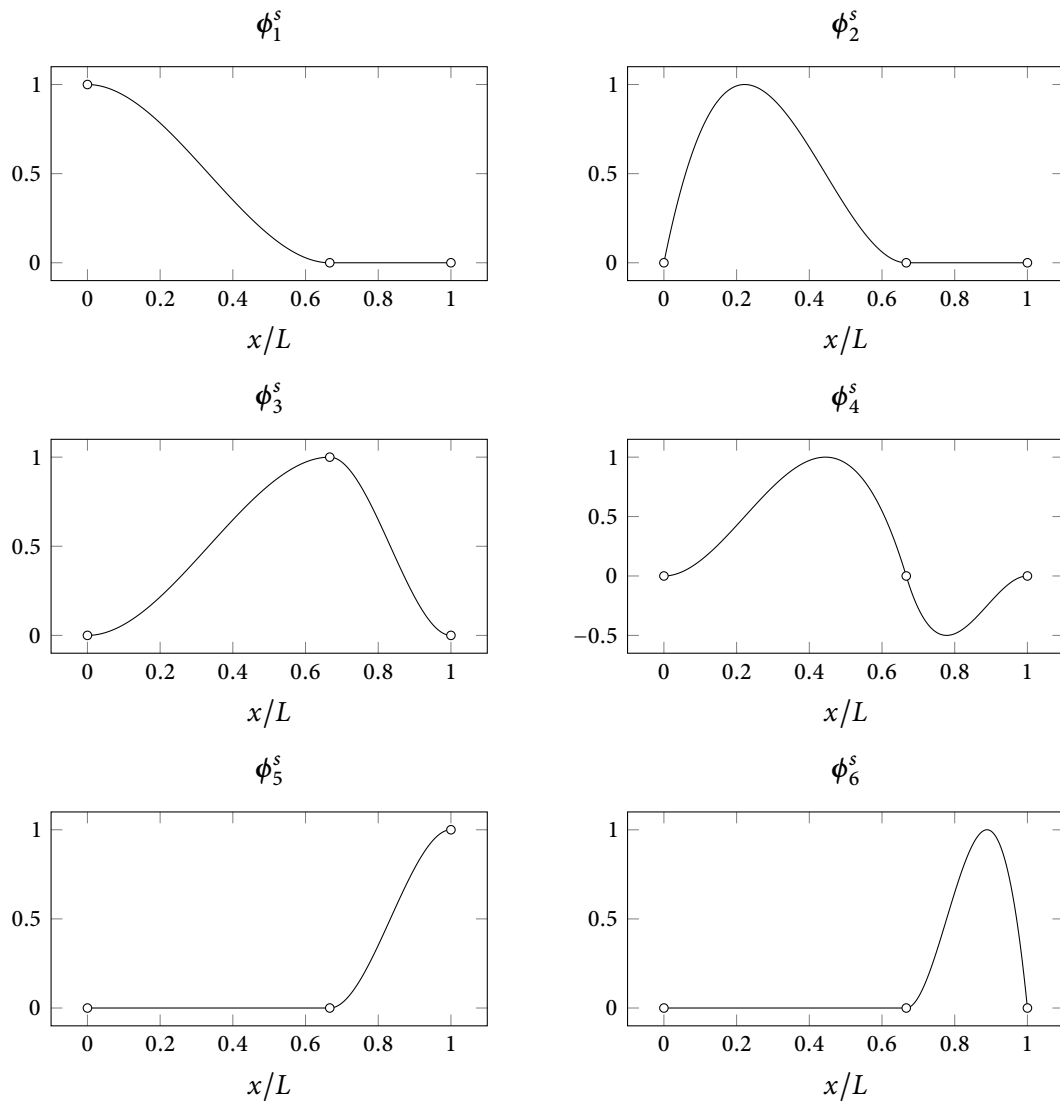


Figure 4.6.: The 6 static modes used in the CRAIG-BAMPTON method.



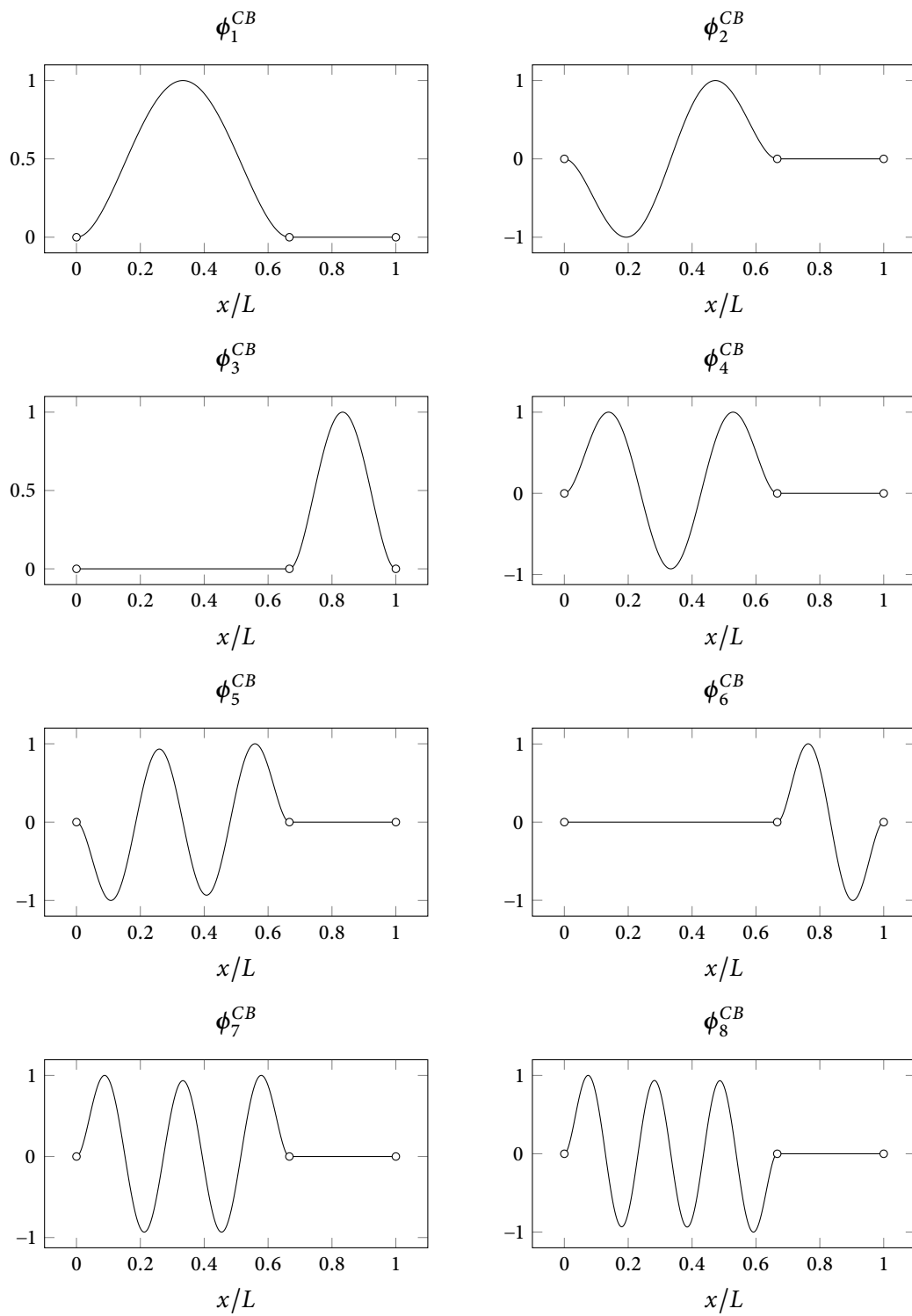


Figure 4.7: First 8 of the 100 eigenmodes used in the CRAIG-BAMPTON method.

### 4.3.3. Preprocessing for the MBS analysis

One can easily see that the modes from Figure 4.6 and 4.7 are not-well suited to describe the motion of either problem beam. This is why there is the need for the MBS preprocessing.

#### Orthogonalisation of the reduced system

First, the system is orthogonalised as described in Section 4.2.1. This is done with the eigenvalue problem stated in Equation (4.18). This problem describes a free floating beam. Since the axial displacements are not possible for the used elements, the beam has two rigid body modes  $\phi_i^r$ . Therefore, the first two eigenvalues of Equation (4.18) are zero. The rigid body modes are shown in Figure 4.8. Figure 4.9 shows the eigenmodes of the free floating beam for the first 8 non-zero eigenvalues.

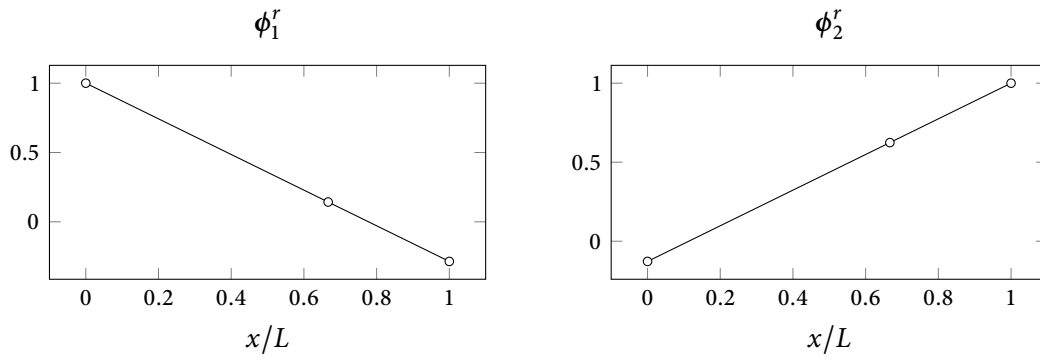


Figure 4.8.: Rigid body modes used for the orthogonalisation of the reduced system.

#### Constrained eigenmodes

To satisfy the boundary conditions for the beams, some of the modes of the free floating beam are made dependent on each other. This is done by mode shifting, see Section 4.2.2. Up to this point, there is no difference in the calculated modes, for example (a) and (b). Table 4.1 states the constrained master DOF for each beam example. In both cases, the dependent modes in the mode shifting procedure are the rigid body modes  $\phi_i^r$ . Figure 4.10 shows the first 8 constrained eigenmodes for beam (a), Figure 4.11 shows them for beam (b). To assess the quality of the constrained eigenmodes, the eigenfrequencies  $\omega_i^c$  are compared with the eigenfrequencies of the full FE model with the same boundary conditions. The relative error for each of the frequencies is shown in Figure 4.12 and 4.13. It can be seen, that up until the last few eigenmodes, the modes represent physical eigenmodes of the beam in a sufficient way, as the error is less than 1%. Also the different boundary conditions do not affect the global type of the error plot. The last couple of modes are non-physical, but still improve the solution as long as their corresponding frequencies

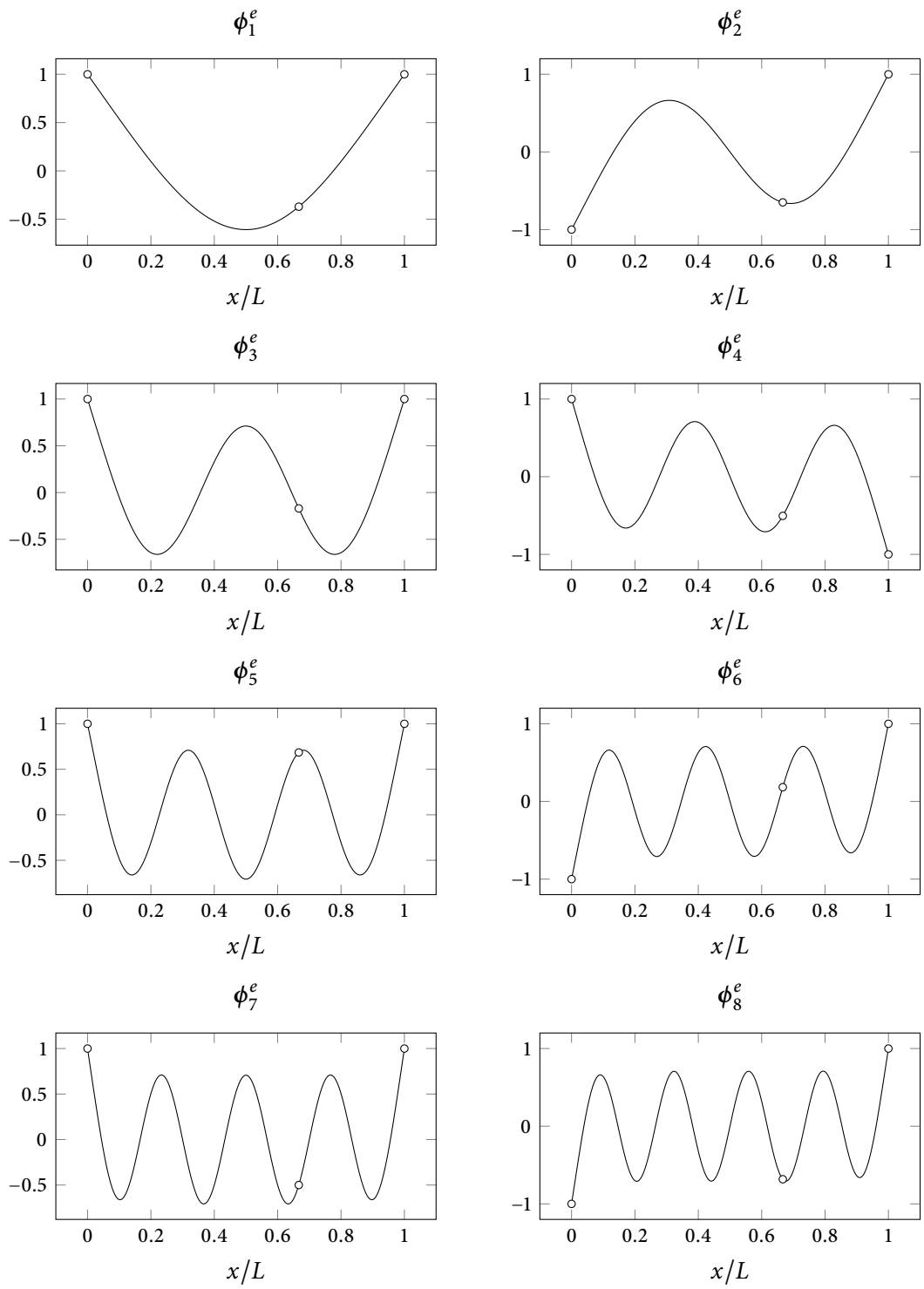


Figure 4.9.: First 8 non-zero eigenmodes used for the orthogonalisation of the reduced system.

are above the characteristic frequencies of the system. If that is not the case, more modes have to be used in the CRAIG–BAMPTON method.

Table 4.1.: Constrained master DOF for each beam problem.

Example beam	constrained master DOF
(a)	1,2
(b)	1,5

### Interface modes

To further reduce the amount of DOF, not all constrained eigenmodes have to be used in the final analysis. For example, if only the modes in a certain frequency spectrum are relevant, only those modes are used in the final analysis. The result can be improved by using more modes with different frequencies or adding interface modes as described in Section 4.2.4. For the two beam examples, frequency response modes are used. FRM are calculated with a frequency  $\Omega_0$ , which can be chosen by the user. As stated before, the standard value in *SIMPACK* is half the first non-zero eigenfrequency of the free floating structure. FRM are most useful at loaded attachment points. The master nodes used are stated in Table 4.2. In Figure 4.12 and 4.13, FRM are shown for different  $\Omega_0$  as well as a different number of constrained eigenmodes  $n_h$  used, where the first  $n_h$  modes are used. For  $n_h = 3$ , small differences in the FRM can be seen, but for a higher number of modes used, the FRM for different  $\Omega_0$  converge. The shape of the FRM varies with the amount of modes used. With more modes used, the FRM seem of a higher order, which is because only higher order modes are available in the  $\mathbf{Q}_n$  matrix and the FRM are calculated as a superposition of the modes in this matrix.

Table 4.2.: Master DOF used to calculate FRM for each beam problem.

Example beam	FRM master DOF
(a)	4
(b)	3

### Harmonic results

To demonstrate the effect of the MBS preprocessing, harmonic results of the undamped system are computed with

$$(-\Omega^2 \mathbf{M}_m + \mathbf{K}_m) \mathbf{u}^h = \mathbf{p}_i^m, \quad (4.58)$$

where  $\mathbf{u}^h$  is the harmonic solution for the displacements and  $\mathbf{p}_i^m$  is the load vector on the final reduced system calculated with

$$\mathbf{p}_i^m = \mathbf{Q}_m^T \mathbf{Q}_c^T \mathbf{Q}_e^T \mathbf{Q}_r^T \mathbf{p}_i. \quad (4.59)$$

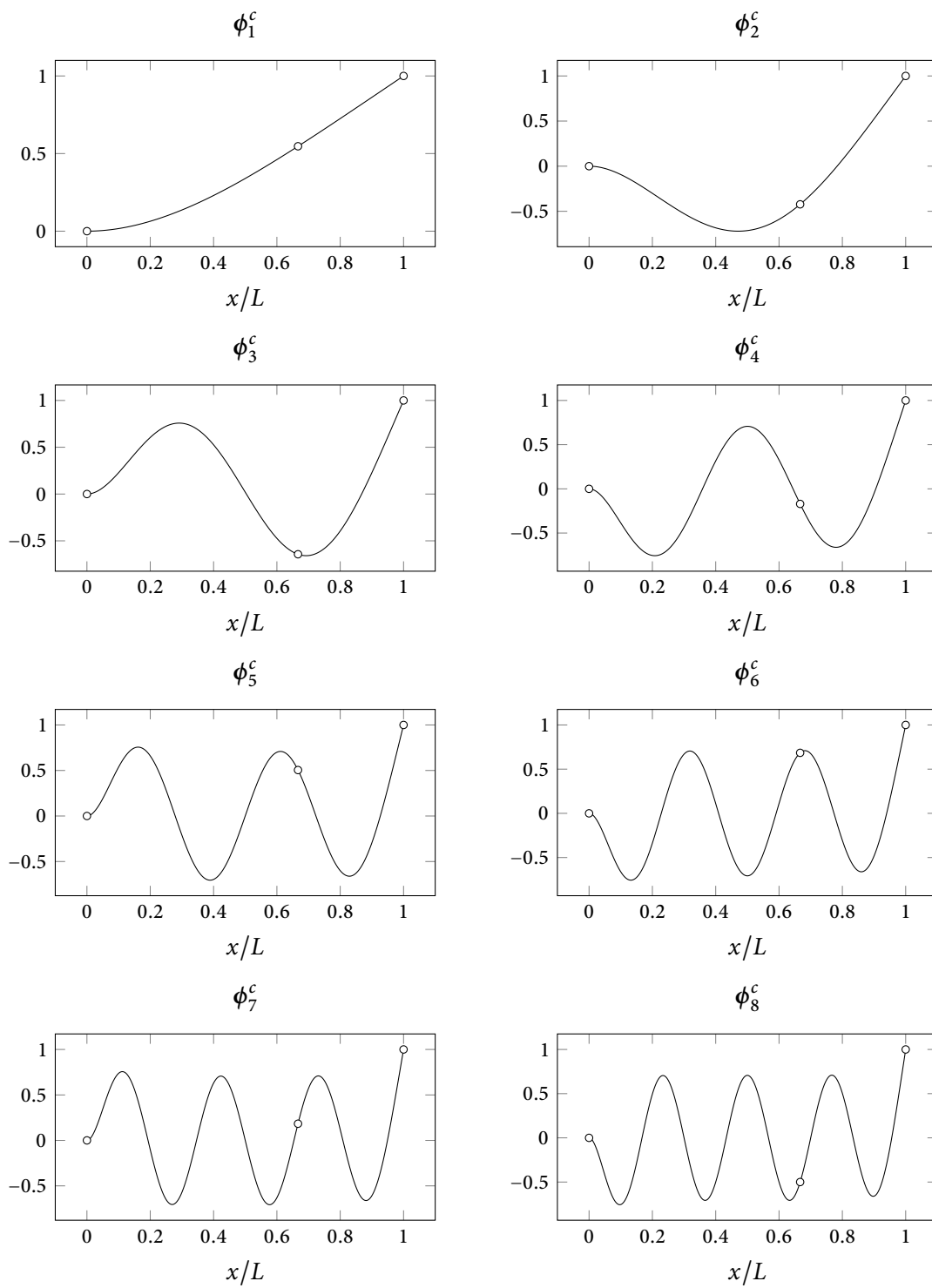


Figure 4.10.: First 8 constrained eigenmodes for the cantilever beam (a).

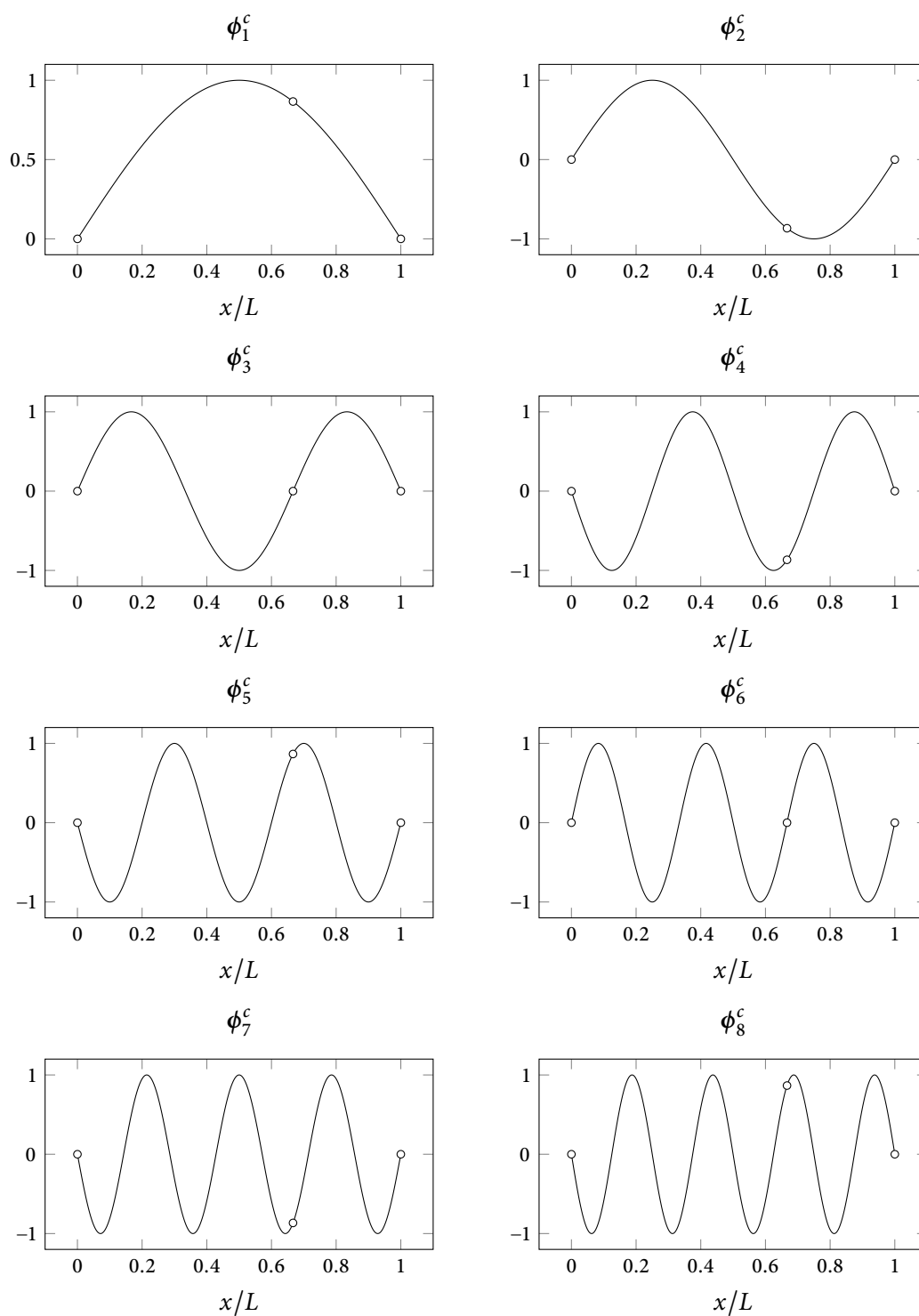


Figure 4.11.: First 8 constrained eigenmodes for the simple supported beam (b).

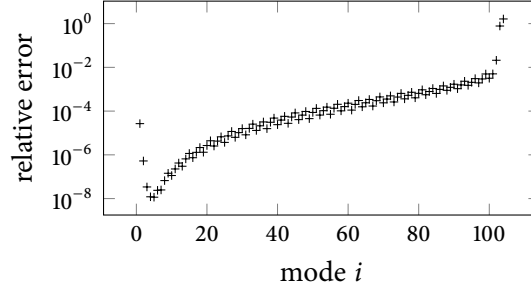


Figure 4.12.: Relative error of the eigenfrequencies  $\omega_i^c$  compared to the eigenfrequencies of the full FE model for beam example (a).

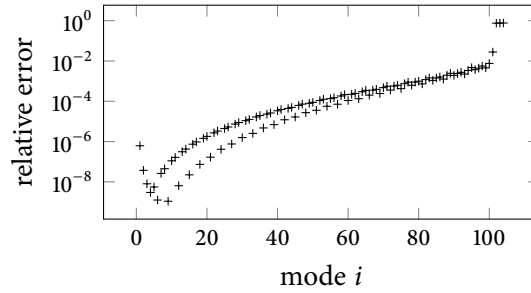


Figure 4.13.: Relative error of the eigenfrequencies  $\omega_i^c$  compared to the eigenfrequencies of the full FE model for beam example (b).

$\mathbf{p}_i$  is the load vector acting on the original beam. The body reference frame does not move. Therefore, there are no additional inertia forces. Equation (4.58) can be solved for  $\mathbf{u}^h$  and from this solution the bending moments and shear forces are calculated. Figure 4.16 and 4.17 show the results for both beam examples with a different number of modes used and FRM compared to the full FE solution. The BERNOULLI-EULER beam elements have cubic interpolation functions for the displacements, therefore the bending moment in one element can be linear and the shear force is constant [14]. For visualisation purposes and because of the high number of beam elements used, the shear force is still shown as a smooth curve and not as piecewise constant lines. For example (a), the result for the displacements is close to the full FE solution with  $n_h = 5$ . To represent the bending moment  $M$ , sufficiently more modes are needed. The shear force  $Q$  cannot be represented with only physical eigenmodes. Using one FRM, the results are already close to the full solution with only 3 modes used, and with 5 modes used the solution is basically the same as the full FE solution. This is because the FRM is calculated with a moment at master node 4 and accounts for the discontinuity at the loading point. In beam example (b), the results are better with the same number of modes because the discontinuity is in the shear force and only results in a kink in the bending moment. With one FRM a similar behaviour as in example (a) can be seen, as the results improve a lot, especially for the section forces. For those two examples, five constrained eigenmodes and one FRM are enough to represent the system. The clear advantage of the MBS model is the size of the system  $6 \times 6$  compared to the  $602 \times 602$  of the full FE system.

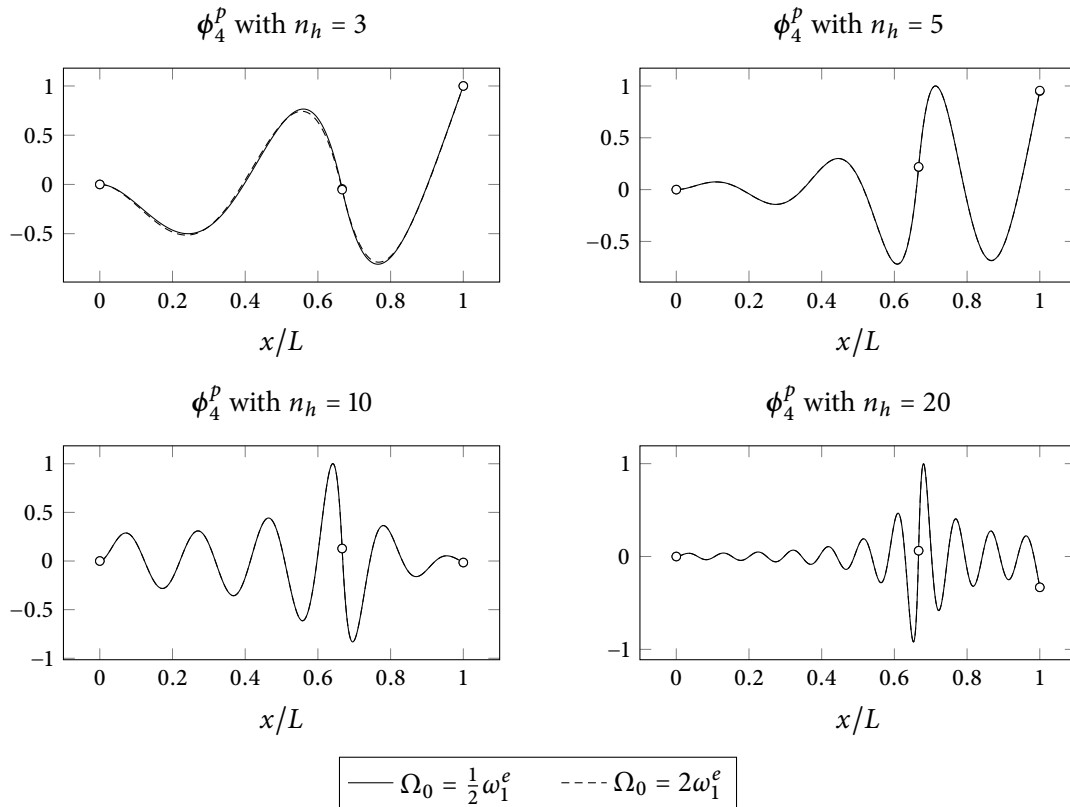


Figure 4.14.: FRM for beam example (a) and different values of  $n_h$  as well as  $\Omega_0$ . The first  $n_h$  modes  $\phi_i^e$  are used for the transformation matrix  $\mathbf{Q}_h$ .



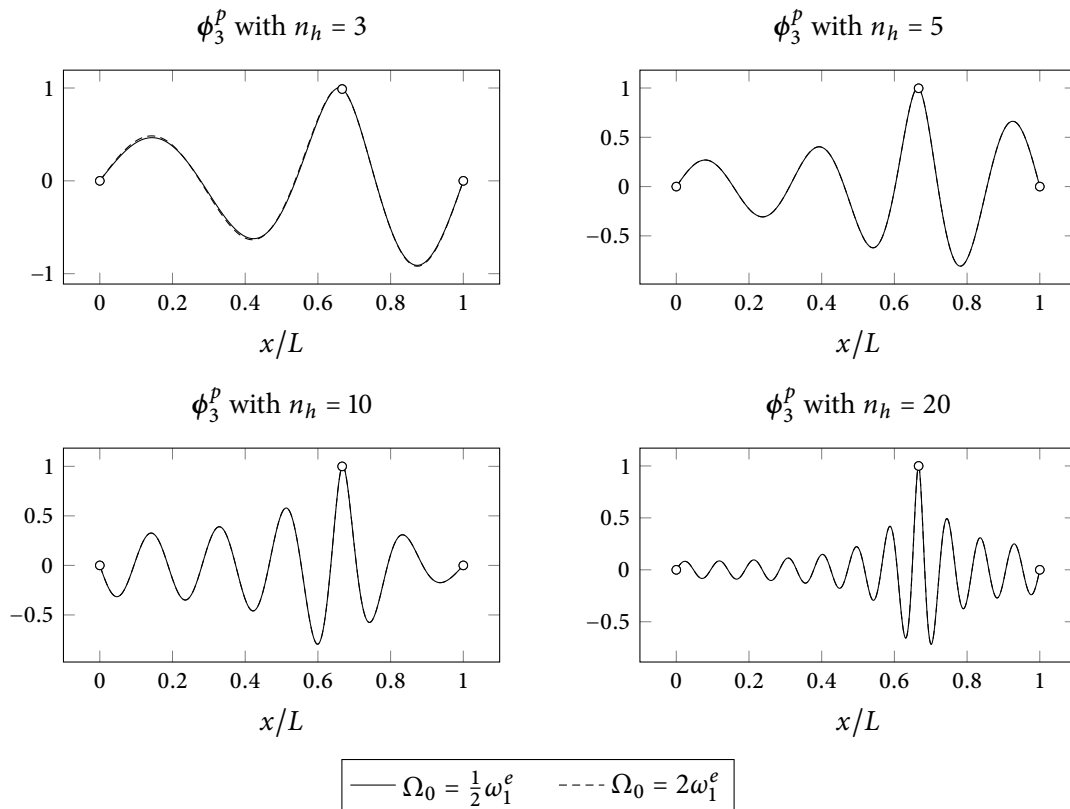


Figure 4.15.: FRM for beam example (b) and different values of  $n_h$  as well as  $\Omega_0$ . The first  $n_h$  modes  $\phi_i^e$  are used for the transformation matrix  $\mathbf{Q}_h$ .

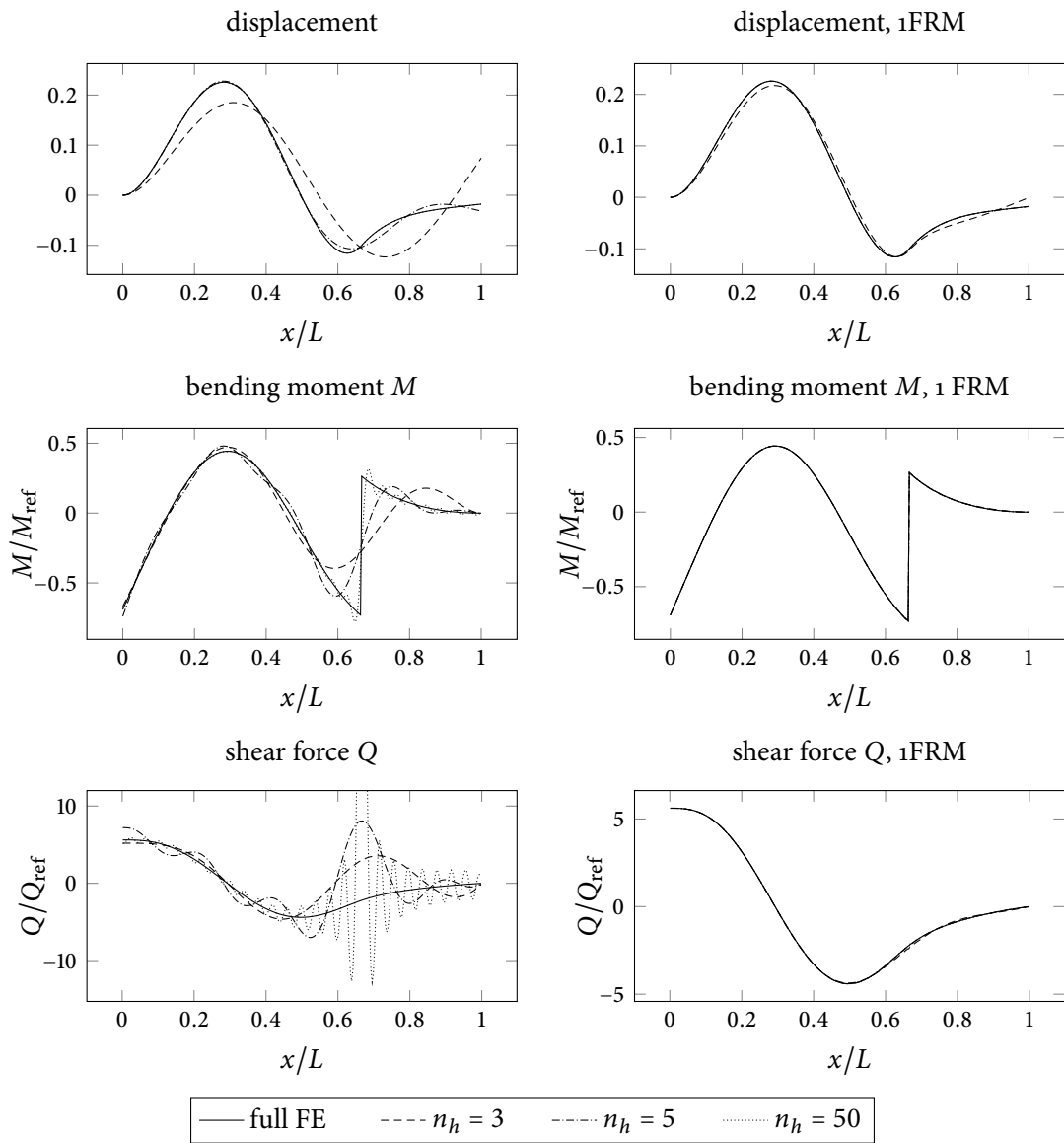


Figure 4.16.: Harmonic results for beam problem (a). The excitation frequency  $\Omega$  is  $3\omega_1^e$ . The plots on the left are calculated with  $n_h$  constrained eigenmodes, the right ones with one additional FRM. The FRM is calculated for master node 4 with the excitation frequency  $\Omega_0 = 1/2\omega_1^e$ . The section forces are scaled with a representative bending moment  $M_{\text{ref}} = M(t)$  and a representative shear force  $Q_{\text{ref}} = M(t)/L$ .

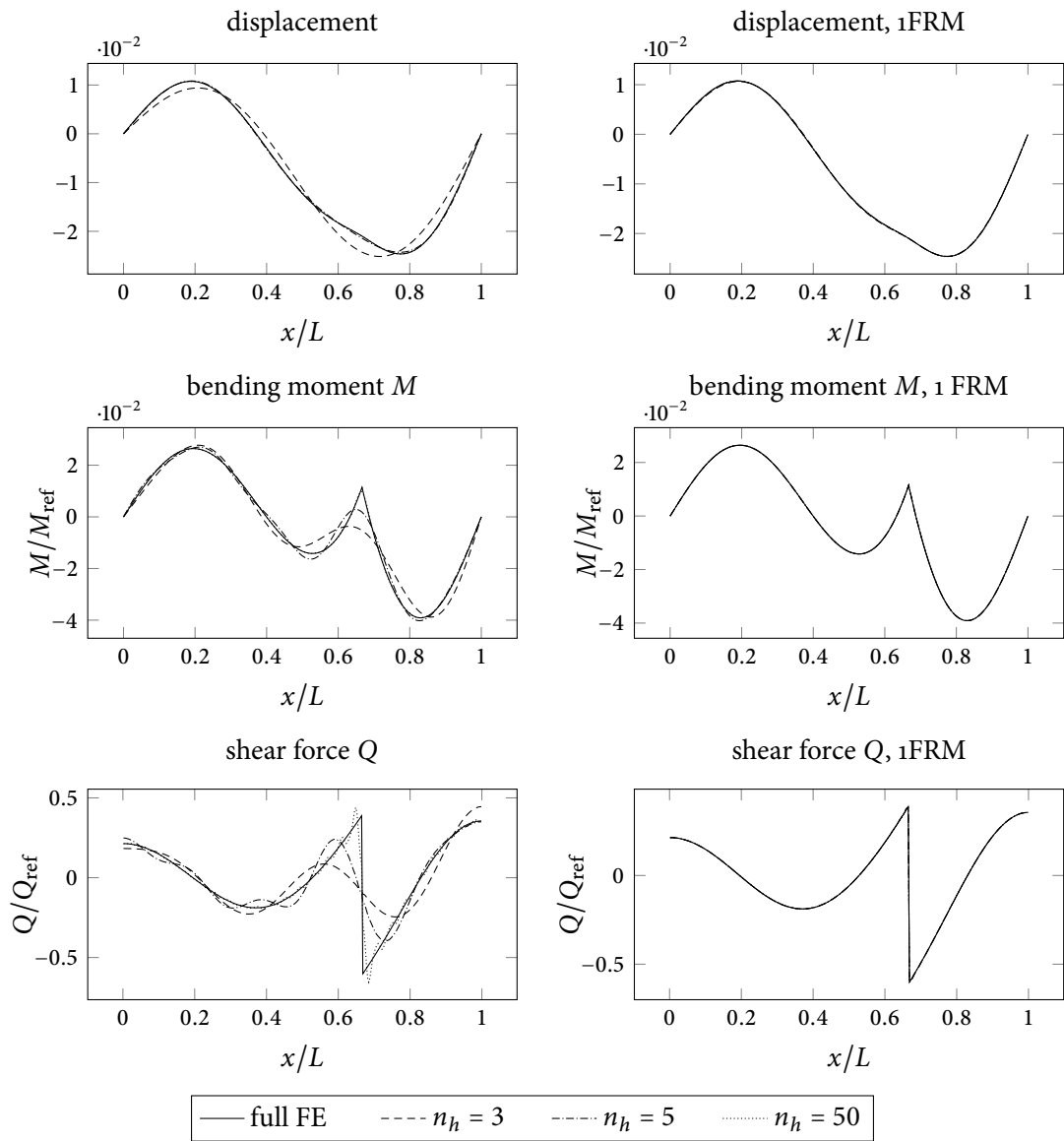


Figure 4.17: Harmonic results for beam problem (b). The excitation frequency  $\Omega = 3\omega_1^e$ . The plots on the left are calculated with  $n_h$  constrained eigenmodes, the right ones with one additional FRM. The FRM is calculated for master node 3 with the excitation frequency  $\Omega_0 = 1/2\omega_1^e$ . The section forces are scaled with a representative bending moment  $M_{\text{ref}} = F(t)L$  and a representative shear force  $Q_{\text{ref}} = F(t)$ .

## 5. Flexible-disc model

The rigid-disc model shows that instabilities of a disc-brake system can occur with a constant friction coefficient. A logical enhancement of the model is to replace the rigid disc with a more realistic flexible disc, shown in Figure 2.5. The deformations of the flexible disc are described by the transversal eigenmodes of the non-rotating disc, where the disc is assumed to be shearstiff. Therefore, the displacement  $w$ , in  $z$  direction, of a point on the mid-surface of the disc is a function of the coordinates  $x$  and  $y$  and time  $t$ . Experiments have shown that when squeal occurs, the disc is vibrating in a mode with three nodal diameters and zero nodal circles, within the frequency range of brake squeal [1]. The disc is assumed to be clamped on the inside and free on the outside. The modes used in the model are the orthogonal eigenmode pair with the form observed in experiments. The scaling factors  $q_1$  and  $q_2$  for the two eigenmodes are the DOF of the model. A constant angular velocity  $\Omega_0$  of the disc in  $z$  direction is assumed. Two point contacts represent the brake pads at the distance  $r_0$  in  $x$  direction. Those brake pads are coupled to the inertial system with a spring  $k$ , and a preload force of  $N_0$  is applied. The assumed contact on the flexible disc is shown in Figure 5.1.  $M$  represents the intersection point between the axis of the brake pads and the mid surface of the disc.  $P$  and  $Q$  are the corresponding points on the upper and lower surface of the disc. They mark a tangent plane on the deformed disc that is used to calculate the contact points  $P'$  and  $Q'$ . Here it is important to at least use quadratic terms in the TAYLOR approximation of the contact points, as otherwise some terms are missing in the linearised equations of motion [1].

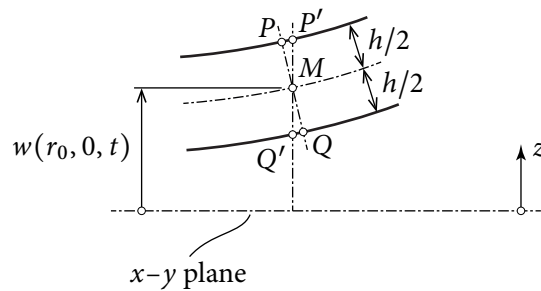


Figure 5.1.: Contact formulation on the flexible disc.

## 5.1. Analytical solution

The analytical solution is given in [1] and since it is quite lengthy, it is not stated here, but the form is very similar to Equation (3.2). Again a non-symmetric stiffness and damping matrix occur. Table 5.1 states the parameters used for the model, the meaning of the parameters for the disc is explained in Section 5.2. The procedure is the same as for the rigid disc and Figure 5.2 shows the real and imaginary parts of the eigenvalues, where the angular velocity  $\Omega_0$  is again varied from  $\Omega_0$  between  $\pi \text{ s}^{-1}$  to  $20\pi \text{ s}^{-1}$ . At  $4.27\pi \text{ s}^{-1}$  one eigenvalue crosses the imaginary axis and the linearised system becomes unstable.

Table 5.1.: Parameters used for the flexible-disc model [4].

Parameter	Physical meaning	Unit	Value
$k$	spring stiffness	N/m	$6 \cdot 10^6$
$N_0$	preload force	N	2000
$\mu$	coefficient of friction	1	0.6
$r_0$	radius for brake pad	m	0.13
$h$	height of the disc	m	0.02
$r_i$	inner radius of the disc	m	0.025
$r_a$	outer radius of the disc	m	0.162
$D$	plate bending stiffness	Nm	67100
$\nu$	POISSON'S ratio	1	0.3
$\gamma$	mass per unit area	$\text{kg/m}^2$	126
$n$	number of nodal diameters	1	3

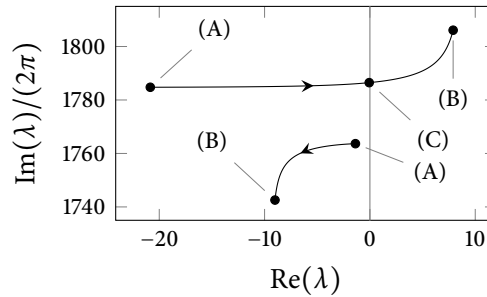


Figure 5.2.: Imaginary and real part of the eigenvalues for the linearised system of the flexible disc. The analytical solution is shown. The angular frequency  $\Omega_0$  varies from  $\pi \text{ s}^{-1}$  to  $20\pi \text{ s}^{-1}$ . Point (A) is calculated with  $\Omega_0 = \pi \text{ s}^{-1}$  and point (B) is calculated with  $\Omega_0 = 20\pi \text{ s}^{-1}$ . Point (C) is at  $\Omega_0 = 4.27\pi \text{ s}^{-1}$  and marks the point where the higher eigenvalue crosses the imaginary axis.

## 5.2. Natural frequencies of a transversely vibrating disc

The equations of motion for a KIRCHHOFF plate are [15]

$$D\Delta\Delta w + \gamma \frac{\partial^2}{\partial t^2} w = 0 \quad (5.1)$$

where  $D$  is a material parameter defined by

$$D = \frac{Eh^3}{12(1-\nu^2)}, \quad (5.2)$$

with YOUNG's modulus  $E$ , POISSON's ratio  $\nu$ , mass per unit area  $\gamma$ , the transversal displacement  $w$  and the plate thickness  $h$ .  $\Delta$  is the LAPLACE operator, in the case of a cylindrical coordinate system given by

$$\Delta = \frac{\partial^2}{\partial r^2} + \frac{1}{r} \frac{\partial}{\partial r} + \frac{1}{r^2} \frac{\partial^2}{\partial \theta^2}. \quad (5.3)$$

In [16], the following solution to Equation (5.1) is assumed

$$w = U(r) \sin(n(\theta - \theta_0)) \sin(\omega(t - t_0)). \quad (5.4)$$

Here  $n$  is the amount of nodal diameters,  $\omega$  is the eigenfrequency and  $U(r)$  is

$$U(r) = C_1 J_n(\beta r) + C_2 Y_n(\beta r) + C_3 I_n(\beta r) + C_4 K_n(\beta r). \quad (5.5)$$

Here  $J_n$  and  $Y_n$  are BESSEL functions of first and second kind,  $I_n$  and  $K_n$  are modified BESSEL functions,  $C_i$  are coefficients and  $\beta$  is defined as

$$\beta^4 = 12(1-\nu^2) \frac{\gamma \omega^2}{Eh^3}. \quad (5.6)$$

The coefficients have to fulfil boundary conditions at the inner and outer edge of the disc. On the outer edge the disc is free, therefore, the bending moment and shear force have to vanish. This gives the equations [16]

$$\frac{\partial^2 w}{\partial r^2} + \nu \left( \frac{1}{r} \frac{\partial w}{\partial r} + \frac{1}{r^2} \frac{\partial^2 w}{\partial \theta^2} \right) = 0 \quad (5.7)$$

$$\frac{\partial}{\partial r} \Delta w + \frac{1-\nu}{r^2} \frac{\partial^2}{\partial \theta^2} \left( \frac{\partial w}{\partial r} - \frac{w}{r} \right) = 0 \quad (5.8)$$

at the outer edge with  $r = r_a$ . On the clamped inner edge with  $r = r_i$ , the displacement and its gradient vanish

$$w = 0 \quad (5.9)$$

$$\frac{\partial w}{\partial r} = 0. \quad (5.10)$$

Equations (5.7–5.8) become lengthy and are not stated here, but they can be found in [16]. The nontrivial solution to the set of equations (5.7–5.10) gives the coefficients  $C_i$  and the parameter  $\beta$ .

With the values given in Table 5.1 the eigenfrequency  $f$  is 1749.75 Hz.

### 5.2.1. Effect of shear flexibility

For various reasons described in Section 5.3.2, the elements used in the FE model take shear flexibility into account. The applied KIRCHHOFF plate theory assumes a shearstiff plate, which is valid if the height of the plate is small compared to its other dimensions. To check if the FE model represents the flexible disc used in the analytical solution, the effect of the shear stiffness is analysed.

Figure 5.3 shows the ratio of the analytical and numerical eigenvalues for a varying ratio of  $r_a/h$ , while the bending stiffness  $D$  and the ratio  $r_a/r_i$  are held constant. It can be seen that for the ratio  $r_a/r_i = 8.1$  considered here, the difference amounts to about 5%. Also, the eigenvalues with shear flexibility are smaller because the system is more flexible. For  $r_a/h \approx 50$  the difference between the analytical and FE model is neglectable. In Figure 5.4 the eigenmodes for the analytical solution and two FE solutions are shown. It is clear that the eigenmodes are not as much effected by a small ratio of  $r_a/h$  as the eigenvalues.

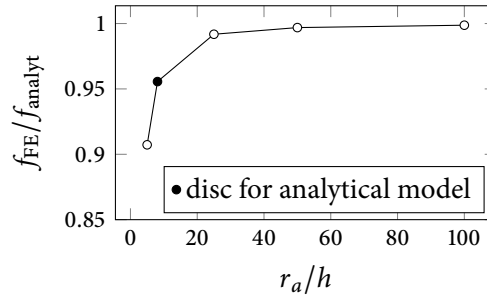


Figure 5.3.: Ratio of the analytical and numerical eigenfrequencies for a varying ratio of  $r_a/h$ . Plate bending stiffness  $D$  and the ratio  $r_a/r_i$  are held constant.

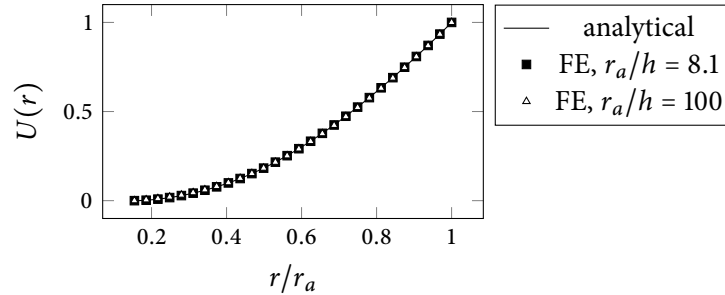


Figure 5.4.: Eigenmode  $U(r)$  of the analytical solution and the FE solution with  $r_a/h = 8.1$  and  $r_a/h = 100$ . Plate bending stiffness  $D$  and the ratio  $r_a/r_i$  are held constant.

## 5.3. MBS simulation

### 5.3.1. Modelling

Due to the contact formulation in the analytical solution essential to model disc-brake squeal, the MBS model is set up similarly. The flexible disc is represented by a disc made out of two dimensional shell elements. The mesh is at the mid surface of the disc. This flexible body is preprocessed with the FE code *ABAQUS*, details of the mesh are described in 5.3.2. The centre node of the disc is fixed to the inertial system with a constant rotation in  $z$  direction. The purpose of this model is to recreate the analytical solution, therefore, only the two eigenmodes with three nodal diameters (cf. [16]) are used as flexible modes for the disc. The corresponding eigenfrequency for those modes is 1672.13 Hz. For further investigations more modes can easily be added to the model. The disc is rotating with respect to the brake-pad axis. Therefore, it is not possible to use one attachment point to model the contact planes as the points rotate. Instead this is done by using a contact element in *SIMPACK* that allows to calculate a line-to-line contact. The calculated contact point represents the intersection of the brake pad axis with the mid surface of the disc. This is possible, because points on the mid surface only move in  $z$  direction. Therefore, the contact point is always on a circle with radius  $r_0$  on the disc, and the attachment points can be modelled accordingly. The force that acts on the disc is then divided and applied to the attachment points near the contact point. The orientation of the marker used in *SIMPACK* to represent the contact point is always orthogonal on the mid surface of the disc. A body with neglectable mass properties is constrained to the contact point and represents an extension to the disc in order to define the contact planes. This is shown in Figure 5.5. With the contact planes now defined, the rest of the model is built up the same way as the rigid-disc model. One difference is that no marker with zero relative velocity is inserted, as contact markers in *SIMPACK* have zero relative velocity towards the body on which they are defined. Therefore the velocities used to calculate the friction force are as if the disc extension would be fixed to the disc. Figure 5.6 shows the topology build-up of the MBS model.

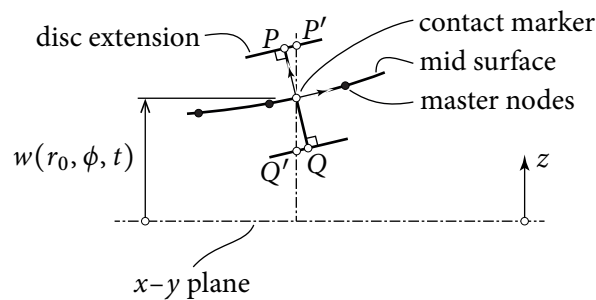


Figure 5.5.: Contact formulation on the flexible disc.



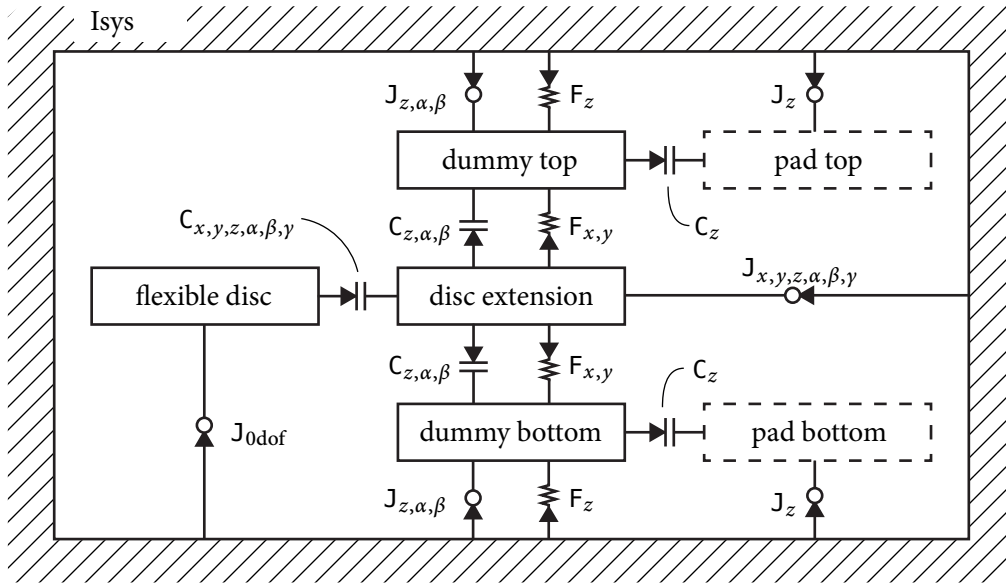


Figure 5.6.: Topology of the MBS flexible-disc model in SIMPACK.

### 5.3.2. FE mesh for the disc

Forces act on the disc at the radius  $r_0$  and the contact element interpolates a contact point between master nodes. Therefore, master nodes are placed on a circle with radius  $r_0$ . Since the main mode of interest has 3 nodal diameters, 60 masters are chosen because for the desired accuracy 20 masters are enough to interpolate one wavelength. To accomplish this, the circular ring on the outside is split up into 60 pieces. This modelling approach is shown in Figure 5.7. One more master node at the centre of the disc is added to fix the disc in the MBS model. This node is kinematically coupled with the nodes on the inner radius  $r_i$ .

The model is meshed with *ABAQUS CAE* and a quad-dominated mesh using 8 node rectangular element S8R and the 6 node triangular element STRI65. Second order elements were chosen to improve accuracy, locking and hourglass properties. Another advantage is that the S8R elements have 6 DOF per node and, therefore, do not require kinematical coupling of the master node rotation normal to the disc, which reduces the complexity of the mesh. The elements used are *thick* shell elements with shear flexibility, which represents a *MINDLIN-REISSNER* plate that is an extension to the *KIRCHHOFF* plate used in the analytical solution. The impact of this discrepancy is discussed in Section 5.2.1. The final mesh is shown in Figure 5.8, it consists of 12120 nodes, 3909 rectangular and 91 triangular elements.

### 5.3.3. Eigenvalues

The analytical and MBS eigenvalues of the rigid-disc model are in good agreement. Yet the results in *SIMPACK* for the flexible disc are completely different from the analytical solution. This is

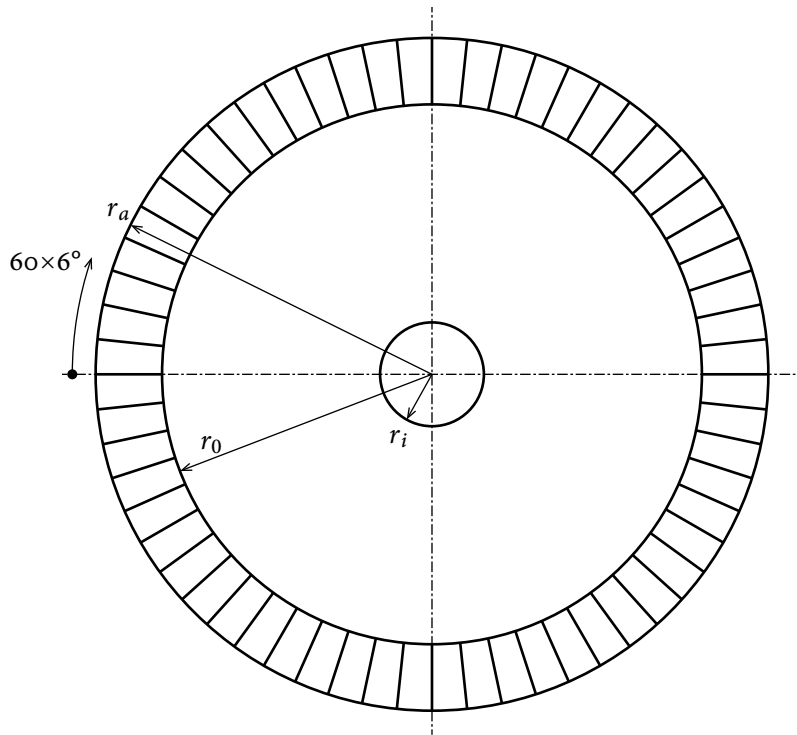


Figure 5.7: Partitioning used for the disc model.

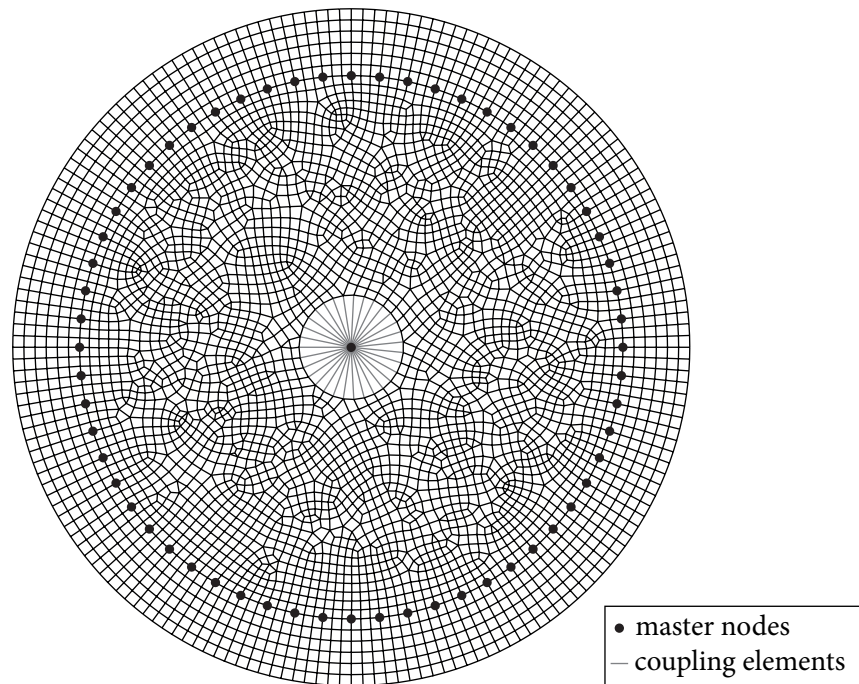


Figure 5.8: Mesh for the flexible disc.

because the eigenvalues in *SIMPACK* only show the expected results if the gradient of all state variables is zero. This is not the case in the flexible-disc model as well as in the rigid-disc model. If all bodies have the same reference system, the results are to some extent as expected. For the rigid-disc model this is the case. On the other hand, the flexible disc is described relative to the body reference frame and the results of the eigenvalue analysis do not have a direct physical interpretation [17].

#### 5.3.4. Transient analysis

Since the model is not suited for an eigenvalue analysis, transient studies of the flexible-disc model are carried out. To obtain a non-zero dynamic response, the flexible position states of both modes are given an imperfection which responds to an initial displacement of the brake pads  $z_P = 6.8 \cdot 10^{-8}$  m. Different analyses are run with varying angular velocities  $\Omega_0$  of the disc and the transient solution is analysed. To simplify the figures, the following plots only show the wrapping curve, see Figure 5.9, of the transient results. Figure 5.10 shows the vertical velocity  $\dot{z}_P$  of the brake pads over time for different values of  $\Omega_0$ .

It can be seen that until  $\Omega_0$  is  $4\pi \text{ s}^{-1}$  the system is stable, from  $4.2\pi \text{ s}^{-1}$  on the response does not decay any more and increases with time. For higher values of  $\Omega_0$  it is clearly visible that the velocity increases exponentially, at least for the time interval shown in the plot. Those observations coincide well with the analytical predictions for the linear system in Section 5.1 where the instability occurs at  $4.269\pi \text{ s}^{-1}$ .

For the general analysis of the system and especially for the concluding acoustic analysis, it is important to know whether if the transient behaviour of the system has a limit cycle. The long time solution for  $\dot{z}_P$  and  $\Omega_0 6\pi \text{ s}^{-1}$  is shown in Figure 5.11a. Up until around 3s the pad velocity  $\dot{z}_P$  increases exponentially, as a linear system would for all times. From 3s to 4.5s the slope decreases and from about 4.5s on the result has reached the limit cycle. Figure 5.11b shows the limit cycle of  $\dot{z}_P$  in detail. The pads oscillate with a single frequency of 1696 Hz, which is slightly above the natural frequency of the disc.

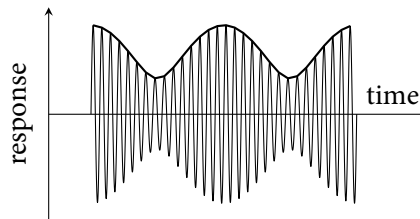


Figure 5.9.: The thin curve is the full time response for a state variable of the system, the thick curve is the wrapping curve used in the following plots.

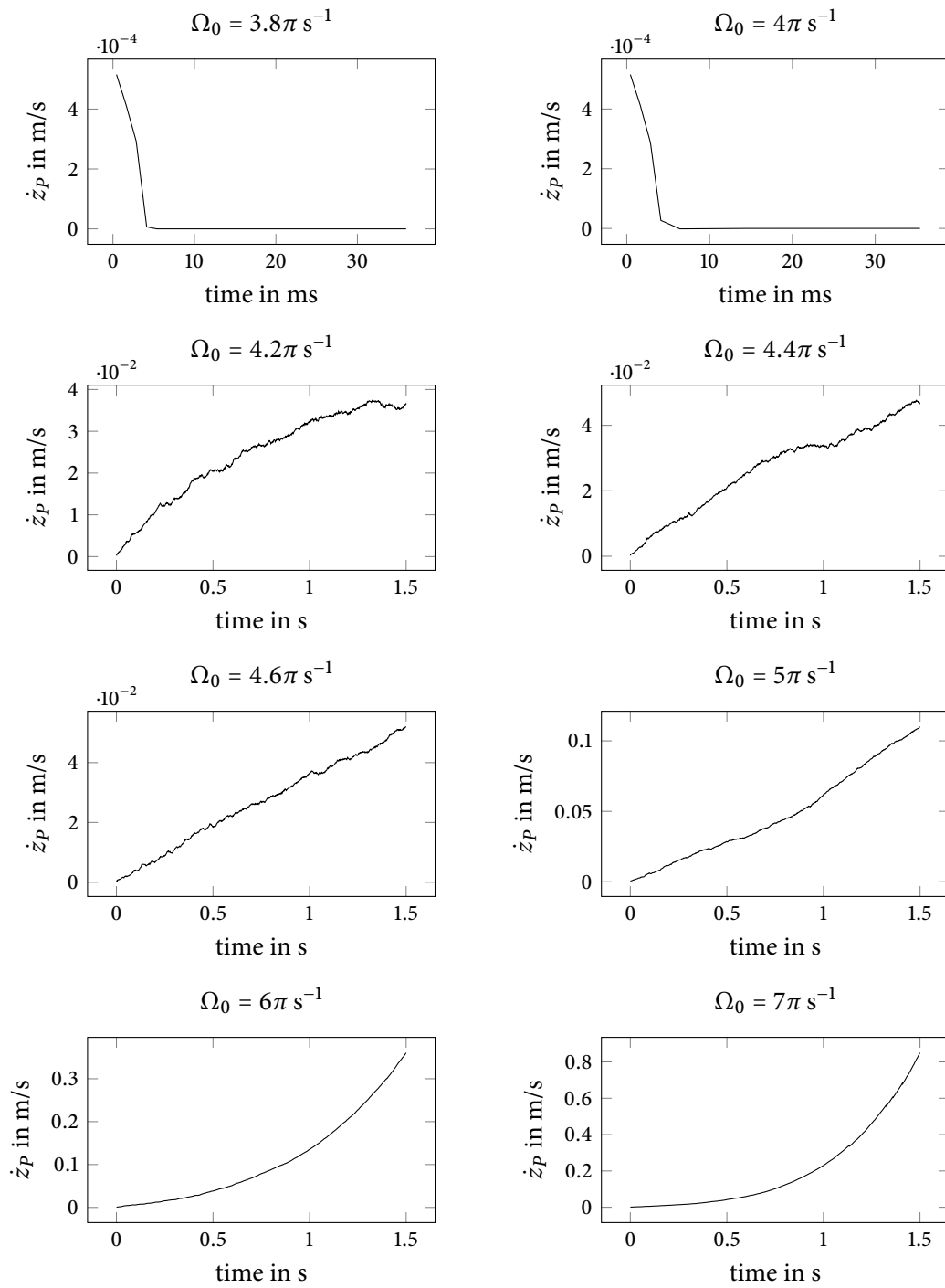


Figure 5.10.: Transient responses of the pad velocity  $\dot{z}_P$  for different values of  $\Omega_0$ . Only the upper wrapping curve, see Figure 5.9, is shown. Note the different scales on the ordinates and the different time units in the first two plots.

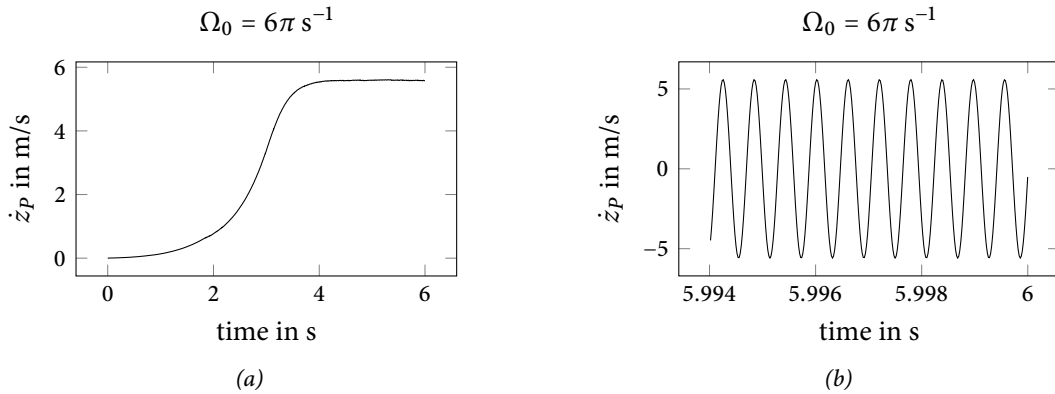


Figure 5.11.: Transient responses of the pad velocity  $\dot{z}_P$  for  $\Omega_0 = 6\pi \text{ s}^{-1}$ . (a) shows the upper wrapping curve, see Figure 5.9. (b) shows the limit cycle in detail.

## 5.4. Acoustic simulation

The results in this section are obtained with support from the *Measurement and Actuator* group of the *Institute of Mechanics and Mechatronics* at the *Vienna University of Technology*. With the research code *CFS++*, an acoustic simulation is performed. The aim of this simulation is a rather qualitative than quantitative solution for the acoustic field surrounding the vibrating brake disc. The only mechanical domain is the brake disc, other elements such as the brake pads and suspension of the brake system are not modelled. The disc is placed in the middle of a cubic air region with an edge length of 1.2 m. Two virtual microphones are added in order to evaluate the sound response. The setup is shown in Figure 5.12. One-way coupling between the mechanical and acoustic field is assumed, with continuous normal velocities at the surface of the disc. The field variable calculated is the acoustic potential  $\psi$  [18]. Results for the normal velocity are taken from the MBS simulation and applied to the boundary interfaces with the air, whereat the rotating eigenmodes from the MBS simulation have to be transferred to non-rotating modes in order to receive the normal velocities for a fixed surface of the disc. Only the limit cycle is simulated with a step time of  $5 \cdot 10^{-5}$  s, which corresponds to 10 steps over a period and 600 transient steps are calculated. For this particular system a harmonic simulation could also be performed.

### 5.4.1. FE model

The acoustic mesh is created with *ANSYS*. In order to get a somewhat structured mesh, the air region is split into several parts, as shown in Figure 5.13. Since the air region is of finite dimensions, the acoustic waves have to be absorbed at the boundaries. For the current simulation this is realised with a *perfectly matched layer (PML)* region outside of the air region (PML). This region is meshed with structured hexahedral (quadratic cubic) elements. The region *AIR\_1* is also meshed with structured hexahedral elements, but with a different size. *DISC* is the mesh on the boundary surfaces of the disc, the relevant mesh is shown in Figure 5.14a. Regions *AIR\_2* and *AIR\_3* are the transition regions between *DISC* and *AIR\_1* and *AIR\_1* and *PML*, respectively. They are meshed

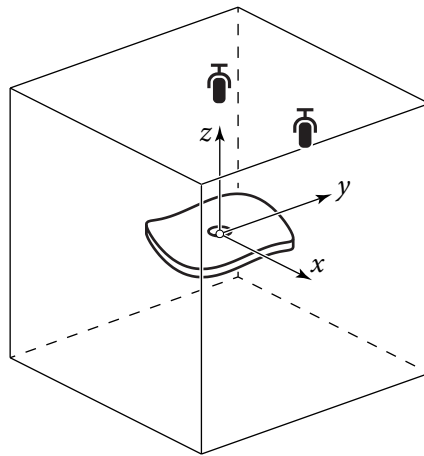


Figure 5.12.: Model setup used for the acoustic simulation.

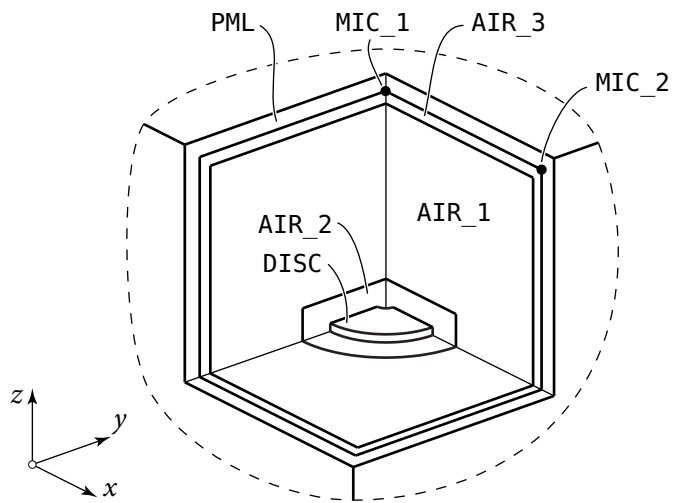


Figure 5.13.: Structuring of the FE model for the acoustic mesh, shown without the fourth octant.

with a hybrid quadratic mesh. This gives a final mesh with about 700,000 elements and 1.7 million nodes. A cut through the final mesh is shown in Figure 5.14b. At the nodes MIC\_1 and MIC\_2, the acoustic pressure is evaluated for Figure 5.16. The acoustic mesh for the disc is different from the mesh used in the MBS analysis, the normal velocity is therefore interpolated from the MBS mesh to the acoustic mesh at each time step.

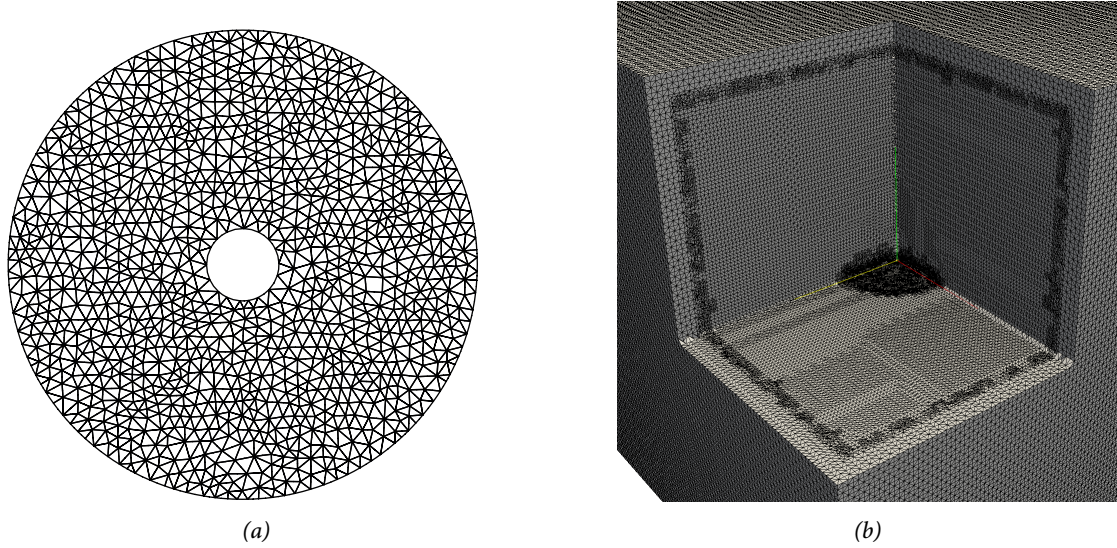


Figure 5.14.: (a) Acoustic mesh of the disc. (b) Final acoustic mesh of the FE model, shown without the grid of the fourth octant (note that the used post-processing software *ParaView* has issues with displaying quadratic elements).

#### 5.4.2. Results

In this section the time derivative of the acoustic potential  $\partial\psi/\partial t$  or the acoustic pressure  $p'$  are discussed. The relation between them is [18]

$$p' = \rho_0 \frac{\partial\psi}{\partial t}, \quad (5.11)$$

where  $\rho_0$  is the density of air. Figure 5.15 shows iso-surfaces of the time derivative of the acoustic potential  $\partial\psi/\partial t$  for a steady state. In the  $x - y$  plane there is almost no acoustic pressure, because the waves from the top and bottom surface of the disc cancel each other out. It can be clearly seen that from the minima/maxima of the disc deformations sound waves emit. Figure 5.16 shows the *fast FOURIER transform (FFT)* of the acoustic potential at the virtual microphones. For the FFT, the transient state at the beginning of the analysis is omitted. For both microphones a peak around 1700 Hz can be clearly seen, which is in good agreement with the vibrations observed in the MBS simulation. The amplitude of the acoustic pressure is about 230 and 380 Pa at MIC\_1 and MIC\_2, respectively. A well known measurement for sound is the *sound pressure level (SPL)*, defined by

$$L_p = 20 \log_{10} \frac{p}{p_{\text{ref}}}, \quad (5.12)$$

with  $p_{\text{ref}} = 20 \mu\text{Pa}$  [18]. The unit of SPL is dB. For the two microphones the SPL is 141 and 145 dB, which is in the range of a gunshot in the distance of 1 m. A more realistic value for the acoustic pressure of brake squeal would be in the single digits, which corresponds to a SPL in the range of 100. The reason for the high values of the acoustic pressure are the simplifications considered in the MBS model of the disc: The flexible disc does not have any damping, which combined with an excitation close to a natural frequency leads to large amplitudes. Furthermore, the only non-linearities included in the model are the friction forces. For example, the spring forces could also be modelled non-linear with a stiffening character as done in [19], which would also lead to smaller amplitudes. Nonetheless, the type of response from the brake disc including structural damping is similar; therefore, the result of the acoustic simulation can be considered to be qualitatively correct.



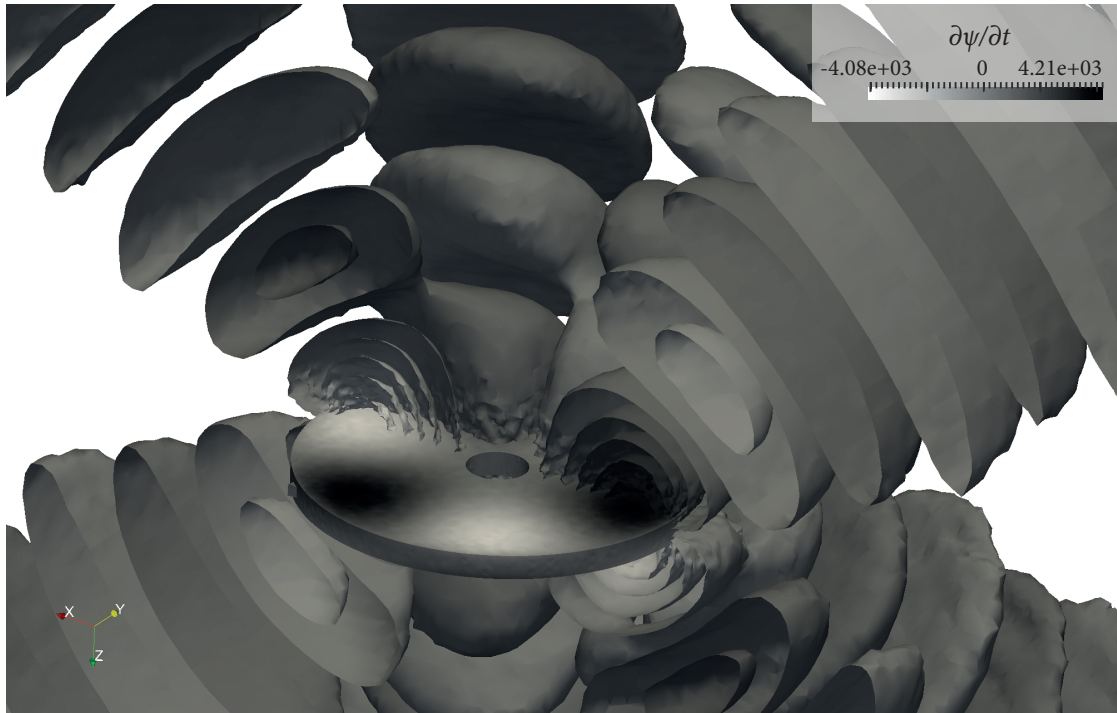


Figure 5.15.: Isosurfaces of the first time derivative of the acoustic potential  $\partial\psi/\partial t$ .

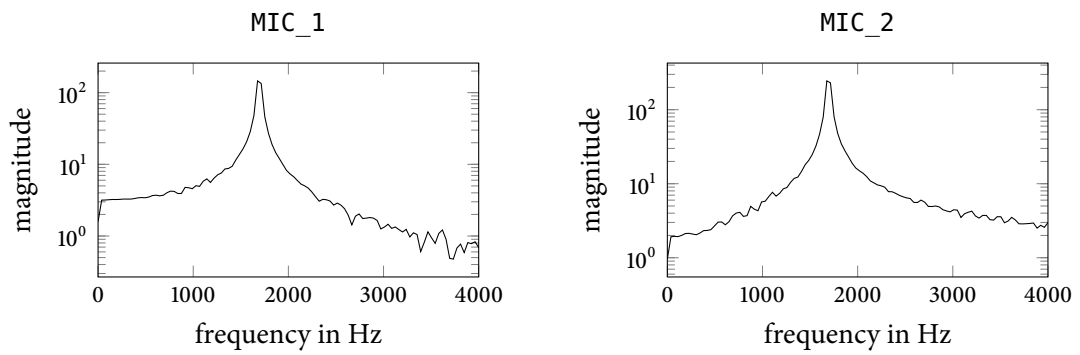


Figure 5.16.: FFT of the acoustic pressure at the virtual microphones.

## 6. Conclusion and outlook

In this work, the suitability of multi-body systems (MBS) to model disc-brake squeal is investigated. It is shown that the commercial MBS software *SIMPACK* is able to map the mechanism used in the rigid- and flexible-disc model from [1, 4] to represent disc-brake squeal in respective minimal models. Those two models are able to model disc-brake squeal without effects such as stick-slip or a velocity dependent coefficient of friction, using only the follower-force characteristics of the friction forces. Both models use point contact between the brake pad and the brake disc. The friction and normal forces are the only sources of instability; therefore, a correct and consistent contact model is the most important part of the modelling. In *SIMPACK* the contact geometry is modelled by using basic geometrical relations rather than complex contact algorithms. This ensures that the contact geometry is exactly as in the analytical models. With the used contact model the analytical results of the eigenvalues for the rigid-disc model can be reproduced in *SIMPACK*. For the flexible-disc model the disc is represented by a finite-element (FE) model which is generated using the commercial FE code *ABAQUS*. In order to get the point on the mid surface where the brake forces act on the flexible disc, a *SIMPACK* contact element is used, but the contact description for the contact between the brake pads and the disc is the same as for the rigid-disc model. It turns out that eigenvalue analysis of moving flexible bodies in *SIMPACK* mostly leads to wrong results due to the internal algorithms. Hence, the flexible disc is given an imperfection and a transient analysis is performed. By doing so, results similar to the analytical model are obtained.

The models generated in *SIMPACK* represent the analytical models. The advantage of the modelling in MBS is that those models can be extended to more complex systems with reasonable effort. A future step is to extend the minimal model. For example, the suspensions of the brake disc and brake pads could be included in order to represent a more realistic brake system. The extension of the point contact to a full surface-to-surface contact seems unrealistic because it is questionable that the used contact algorithms are able to represent the contact in a sufficient way for the self-excited vibrations to occur [1] – surface-to-surface contact might be more suited for a respective FE analysis. A more promising MBS approach is to discretise the contact surface with a grid of point contacts as used in this thesis. This ensures the correct contact description and gives a more realistic model of the brake system.

In order to include the flexible disc into *SIMPACK* the disc is modelled with FE and then processed into a MBS suitable form. The detailed steps from a FE model to a flexible body in MBS are stated. It is shown that the FE model of a mechanical structure only needs to be reduced once and can be used for different boundary conditions. Therefore, the user can test various boundary conditions in the MBS analysis without having to redo the computationally expensive FE reduction, only mode shifting and the subsequent procedures in the MBS preprocessing have to be

recalculated, but due to the small system this is computationally fast. Based on the modes used in the FE reduction, the MBS preprocessing generates suitable coordinate transformations to calculate constrained modes that represent the physical eigenmodes of the constrained structure. The user can decide which modes to use in the final analysis. This should be done with caution as the computational time increases with the number of modes, but skipping relevant modes might lead to dissatisfying results. Especially if stresses are analysed, frequency response modes (FRM) should be used as they improve the solution dramatically compared to adding additional eigenmodes. If all available modes of the CRAIG–BAMPTON method are used, the only way to improve the solution is to redo the FE reduction with more CRAIG–BAMPTON modes.

Conclusively the results of the MBS simulation of the flexible disc are used to carry out an acoustic FE simulation. It is shown that the sound waves emitted by the disc can be simulated. With further advanced MBS models and a more realistic acoustic simulation setup this approach seems promising. In doing so, the actual acoustic response of brake squeal can be simulated in the early development stages of a brake system, and measures can be taken in order to reduce the perceived noise of the squeal.

## A. SIMPACK

The software package *SIMPACK* is used to model the MBS presented in this thesis. This chapter is a short explanation of the framework and terminology used in *SIMPACK*. Figure A.1 shows the notation for displacements and rotations in three dimensions used in *SIMPACK*. A *SIMPACK* model consists of bodies that interact with each other. Markers are coordinate systems that can be defined on any body. Table A.1 shows the symbols used for the described *SIMPACK* elements. The arrow denotes which is the *from* and which is the *to* marker. The directions given for the elements refer to the *from* marker. The described *SIMPACK* elements always connect one marker to another. Each non-flexible body has six DOF and one joint element. The joint element defines the minimal coordinates for the body and restricts its movement. Each body has exactly one joint and it has to be defined. For example, a computer mouse would have a planar joint restricting the movement normal to the surface and only allowing rotation perpendicular to the surface. This joint would be written as  $J_{x,y,y}$ , where the indices refer to the remaining DOF. The joint of a body can only be linked to one other body or the inertial system. Bodies can be coupled to other bodies with force and constraint elements. Constraint elements restrict the movement of a body compared to another body or the inertial system. The joint used for the computer mouse could also be modelled with a constraint restricting the movement in  $z$  direction and the rotation in  $x$  and  $y$  direction. This would be written as  $C_{z,\alpha,\beta}$ , where the indices refer to the constrained DOF. Force elements do not restrict movement, they apply force on bodies such as spring forces, damper forces, friction forces, external loads, etc. A force element is written as  $J_{x,y,z,\alpha,\beta,\gamma}$  where the indices refer to the directions in which a force acts.

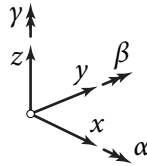


Figure A.1.: Notation for displacements and rotations used in *SIMPACK*.

Table A.1.: Symbols for *SIMPACK* modelling elements.

Symbol	identifier	<i>SIMPACK</i> element
$\rightarrow \circ \leftarrow$	$J_{x,y,z,\alpha,\beta,\gamma}$	joint
$\rightarrow \parallel \leftarrow$	$C_{x,y,z,\alpha,\beta,\gamma}$	constraint
$\rightarrow \circ \leftarrow$	$F_{x,y,z,\alpha,\beta,\gamma}$	force

## B. Transformation of coordinates

Let the equations of motion for a system be

$$M\ddot{\mathbf{q}} + C\dot{\mathbf{q}} + K\mathbf{q} = \mathbf{f}, \quad (\text{B.1})$$

where  $\mathbf{q}$  is the state vector. A new set of state variables  $\bar{\mathbf{q}}$  is introduced, with the relation

$$\mathbf{q} = Q\bar{\mathbf{q}}, \quad (\text{B.2})$$

where  $Q$  is a constant transformation matrix. Now Equation (B.1) is multiplied with the transposed virtual state vector  $\delta\mathbf{q}^T$  from the left side

$$\delta\mathbf{q}^T M\ddot{\mathbf{q}} + \delta\mathbf{q}^T C\dot{\mathbf{q}} + \delta\mathbf{q}^T K\mathbf{q} = \delta\mathbf{q}^T \mathbf{f}. \quad (\text{B.3})$$

Equation (B.2) inserted into (B.3) yields

$$\delta\bar{\mathbf{q}}^T Q^T M Q \ddot{\bar{\mathbf{q}}} + \delta\bar{\mathbf{q}}^T Q^T C Q \dot{\bar{\mathbf{q}}} + \delta\bar{\mathbf{q}}^T Q^T K Q \bar{\mathbf{q}} = \delta\bar{\mathbf{q}}^T Q^T \mathbf{f}. \quad (\text{B.4})$$

Every entry of  $\delta\bar{\mathbf{q}}$  can be chosen individually and therefore the scalar Equation (B.4) is equivalent with the vector equation

$$Q^T M Q \ddot{\bar{\mathbf{q}}} + Q^T C Q \dot{\bar{\mathbf{q}}} + Q^T K Q \bar{\mathbf{q}} = Q^T \mathbf{f}. \quad (\text{B.5})$$

This can be written as

$$\bar{M}\ddot{\bar{\mathbf{q}}} + \bar{C}\dot{\bar{\mathbf{q}}} + \bar{K}\bar{\mathbf{q}} = \bar{\mathbf{f}}, \quad (\text{B.6})$$

with the transformed system matrices and force vector

$$\bar{M} = Q^T M Q \quad (\text{B.7})$$

$$\bar{C} = Q^T C Q \quad (\text{B.8})$$

$$\bar{K} = Q^T K Q \quad (\text{B.9})$$

$$\bar{\mathbf{f}} = Q^T \mathbf{f}. \quad (\text{B.10})$$

(B.6) is the transformed equation of motion. If  $Q$  is invertible, the transformed system is equivalent to the original one. For a non-invertible transformation matrix, the transformed system only gives an approximation of the full system. A good choice of the transformation matrix for the given system gives an approximation close to the real solution.

# List of Figures

2.1.	(a) Friction characteristic used by the SHIN model [4]. (b) Model by SHIN <i>et al.</i> [4].	4
2.2.	Model by POPP <i>et al.</i> [4]. . . . .	4
2.3.	Model by BROMMUNDT [4]. . . . .	4
2.4.	Rigid-disc model by VONWAGNER <i>et al.</i> [4]. . . . .	5
2.5.	Flexible-disc model by HOCHLENERT <i>et al.</i> . . . . .	5
2.6.	Contact geometry used in the MBS model. . . . .	7
3.1.	Imaginary and real part of the eigenvalues for the linearised system of the rigid disc. The analytical solution is shown. The angular frequency $\Omega_0$ varies from $\pi \text{ s}^{-1}$ to $20\pi \text{ s}^{-1}$ . Point (A) is calculated with $\Omega_0 = \pi \text{ s}^{-1}$ and point (B) is calculated with $\Omega_0 = 20\pi \text{ s}^{-1}$ . Point (C) is at $\Omega_0 = 10.4\pi \text{ s}^{-1}$ and marks the point where the motion of the disc becomes unstable. . . . .	9
3.2.	Topology of the MBS rigid-disc model in <i>SIMPACK</i> . . . . .	10
3.3.	Imaginary and real part of the eigenvalues for the linearised system of the rigid disc. The analytical as well as two different MBS results are shown. The angular frequency $\Omega_0$ is varied from $\pi \text{ s}^{-1}$ to $20\pi \text{ s}^{-1}$ . Point (A) is calculated with $\Omega_0 = \pi \text{ s}^{-1}$ and point (B) is calculated with $\Omega_0 = 20\pi \text{ s}^{-1}$ . . . . .	11
4.1.	Simple supported beam with superposition of two eigenmodes. . . . .	12
4.2.	Floating flexible body in two dimensions. . . . .	13
4.3.	Workflow for FE preparation of flexible bodies using the CRAIG-BAMPTON reduction method in the FE program and a MBS preprocessing similar to the one used in <i>SIMPACK</i> . . . . .	14
4.4.	The two example problems. . . . .	23
4.5.	Numbering of the master DOF for the reduced model. . . . .	23
4.6.	The 6 static modes used in the CRAIG-BAMPTON method. . . . .	24
4.7.	First 8 of the 100 eigenmodes used in the CRAIG-BAMPTON method. . . . .	25
4.8.	Rigid body modes used for the orthogonalisation of the reduced system. . . . .	26
4.9.	First 8 non-zero eigenmodes used for the orthogonalisation of the reduced system. . . . .	27
4.10.	First 8 constrained eigenmodes for the cantilever beam (a). . . . .	29
4.11.	First 8 constrained eigenmodes for the simple supported beam (b). . . . .	30
4.12.	Relative error of the eigenfrequencies $\omega_i^c$ compared to the eigenfrequencies of the full FE model for beam example (a). . . . .	31
4.13.	Relative error of the eigenfrequencies $\omega_i^c$ compared to the eigenfrequencies of the full FE model for beam example (b). . . . .	31

4.14.	FRM for beam example (a) and different values of $n_h$ as well as $\Omega_0$ . The first $n_h$ modes $\phi_i^c$ are used for the transformation matrix $\mathbf{Q}_h$ . . . . .	32
4.15.	FRM for beam example (b) and different values of $n_h$ as well as $\Omega_0$ . The first $n_h$ modes $\phi_i^c$ are used for the transformation matrix $\mathbf{Q}_h$ . . . . .	33
4.16.	Harmonic results for beam problem (a). The excitation frequency $\Omega$ is $3\omega_1^e$ . The plots on the left are calculated with $n_h$ constrained eigenmodes, the right ones with one additional FRM. The FRM is calculated for master node 4 with the excitation frequency $\Omega_0 = 1/2\omega_1^e$ . The section forces are scaled with a representative bending moment $M_{\text{ref}} = M(t)$ and a representative shear force $Q_{\text{ref}} = M(t)/L$ . . . . .	34
4.17.	Harmonic results for beam problem (b). The excitation frequency $\Omega$ is $3\omega_1^e$ . The plots on the left are calculated with $n_h$ constrained eigenmodes, the right ones with one additional FRM. The FRM is calculated for master node 3 with the excitation frequency $\Omega_0 = 1/2\omega_1^e$ . The section forces are scaled with a representative bending moment $M_{\text{ref}} = F(t)L$ and a representative shear force $Q_{\text{ref}} = F(t)$ . . . . .	35
5.1.	Contact formulation on the flexible disc. . . . .	36
5.2.	Imaginary and real part of the eigenvalues for the linearised system of the flexible disc. The analytical solution is shown. The angular frequency $\Omega_0$ varies from $\pi\text{s}^{-1}$ to $20\pi\text{s}^{-1}$ . Point (A) is calculated with $\Omega_0 = \pi\text{s}^{-1}$ and point (B) is calculated with $\Omega_0 = 20\pi\text{s}^{-1}$ . Point (C) is at $\Omega_0 = 4.27\pi\text{s}^{-1}$ and marks the point where the higher eigenvalue crosses the imaginary axis. . . . .	37
5.3.	Ratio of the analytical and numerical eigenfrequencies for a varying ratio of $r_a/h$ . Plate bending stiffness $D$ and the ratio $r_a/r_i$ are held constant. . . . .	39
5.4.	Eigenmode $U(r)$ of the analytical solution and the FE solution with $r_a/h = 8.1$ and $r_a/h = 100$ . Plate bending stiffness $D$ and the ratio $r_a/r_i$ are held constant. . . . .	39
5.5.	Contact formulation on the flexible disc. . . . .	40
5.6.	Topology of the MBS flexible-disc model in SIMPACK. . . . .	41
5.7.	Partitioning used for the disc model. . . . .	42
5.8.	Mesh for the flexible disc. . . . .	42
5.9.	The thin curve is the full time response for a state variable of the system, the thick curve is the wrapping curve used in the following plots. . . . .	43
5.10.	Transient responses of the pad velocity $\dot{z}_P$ for different values of $\Omega_0$ . Only the upper wrapping curve, see Figure 5.9, is shown. Note the different scales on the ordinates and the different time units in the first two plots. . . . .	44
5.11.	Transient responses of the pad velocity $\dot{z}_P$ for $\Omega_0 = 6\pi\text{s}^{-1}$ . (a) shows the upper wrapping curve, see Figure 5.9. (b) shows the limit cycle in detail. . . . .	45
5.12.	Model setup used for the acoustic simulation. . . . .	46
5.13.	Structuring of the FE model for the acoustic mesh, shown without the fourth octant. . . . .	46
5.14.	(a) Acoustic mesh of the disc. (b) Final acoustic mesh of the FE model, shown without the grid of the fourth octant (note that the used post-processing software <i>ParaView</i> has issues with displaying quadratic elements). . . . .	47
5.15.	Isosurfaces of the first time derivative of the acoustic potential $\partial\psi/\partial t$ . . . . .	49
5.16.	FFT of the acoustic pressure at the virtual microphones. . . . .	49

A.1. Notation for displacements and rotations used in *SIMPACK*. . . . . 52



# List of Tables

3.1.	Parameters used for the rigid-disc model [4]. . . . .	9
4.1.	Constrained master DOF for each beam problem. . . . .	28
4.2.	Master DOF used to calculate FRM for each beam problem. . . . .	28
5.1.	Parameters used for the flexible-disc model [4]. . . . .	37
A.1.	Symbols for <i>SIMPACK</i> modelling elements. . . . .	52

# Bibliography

- [1] D. Hochlenert. *Selbsterregte Schwingungen in Scheibenbremsen: Mathematische Modellbildung und aktive Unterdrückung von Bremsenquietschen*. Shaker, 2006.
- [2] C. Cantoni et al. “Brake comfort—a review”. In: *Vehicle System Dynamics* 47.8 (2009), pp. 901–947.
- [3] Y. Dai and T. C. Lim. “Suppression of brake squeal noise applying finite element brake and pad model enhanced by spectral-based assurance criteria”. In: *Applied Acoustics* 69.3 (2008), pp. 196–214.
- [4] U. von Wagner, D. Hochlenert, and P. Hagedorn. “Minimal models for disk brake squeal”. In: *Journal of Sound and Vibration* 302.3 (2007), pp. 527–539.
- [5] K. Popp and P. Stelzer. “Stick-slip vibrations and chaos”. In: *Philosophical Transactions of the Royal Society of London. Series A: Physical and Engineering Sciences* 332.1624 (1990), pp. 89–105.
- [6] K. Shin et al. “Analysis of disc brake noise using a two-degree-of-freedom model”. In: *Journal of Sound and Vibration* 254.5 (2002), pp. 837–848.
- [7] K. Popp et al. “Mechanisms to generate and to avoid friction induced vibrations”. In: *VDI-Bericht, Vol. 1736* (2002).
- [8] E. Brommundt. “Ein Reibschwinger mit Selbsterregung ohne fallende Reibkennlinie”. In: *ZAMM - Journal of Applied Mathematics and Mechanics* 75.12 (1995), pp. 811–820. ISSN: 1521-4001.
- [9] D. Hochlenert, G. Spelsberg-Korspeter, and P. Hagedorn. “Friction induced vibrations in moving continua and their application to brake squeal”. In: *Journal of Applied Mechanics* 74.3 (2007), pp. 542–549.
- [10] SIMPACK Reference Manual. *Release 9.6*. SIMPACK AG. Wessling, Germany, 2014.
- [11] S. Dietz. “Vibration and fatigue analysis of vehicle systems using component modes”. In: *Fortschritt Berichte-VDI Reihe 12 Verkehrstechnik Fahrzeugtechnik* (1999).
- [12] R. R. Craig and M. C. C. Bampton. “Coupling of substructures for dynamic analyses”. In: *AIAA Journal* 6.7 (1968), pp. 1313–1319.
- [13] R. J. Guyan. “Reduction of stiffness and mass matrices”. In: *AIAA Journal* 3.2 (1965), pp. 380–380.
- [14] R. D. Cook et al. *Concepts and Applications of Finite Element Analysis, 4th Edition*. 4th ed. Wiley, Oct. 2001. ISBN: 0471356050.

- [15] A. W. Leissa. *Vibration of Plates*. NASA SP. Scientific, Technical Information Division, National Aeronautics, and Space Administration, 1969.
- [16] S.M. Vogel and D.W. Skinner. “Natural frequencies of transversely vibrating uniform annular plates”. In: *Journal of Applied Mechanics* 32.4 (1965), pp. 926–931.
- [17] T. Liebernickel. Personal e-mail communication, support SIMPACK AG. Feb. 26, 2015.
- [18] M. Kaltenbacher. *Numerical Simulation of Mechatronic Sensors and Actuators: Finite Elements for Computational Multiphysics*. Springer Berlin Heidelberg, 2015. ISBN: 9783642401701.
- [19] D. Hochlenert. “Nonlinear stability analysis of a disk brake model”. In: *Nonlinear Dynamics* 58.1-2 (2009), pp. 63–73.